MASTER

DOE/ER/03158--74

DIRECT OBSERVATION OF THE PRIMARY STATE OF DAMAGE OF ION-IRRADIATED TUNGSTEN: I. THREE-DIMENSIONAL SPATIAL DISTRIBUTION OF VACANCIES

by

Ching-Yeu Wei, Michael I. Current and
David N. Seidman

October 1980

Report #4235

Issued by
The Materials Science Center

Prepared for
THE U.S. DEPARTMENT OF ENERGY
UNDER CONTRACT NO. DE-AC02-76ER03158

DISTRIBUTION OF THIS DOCUMENT IS UNLIMITED

DISCLAIMER

DIRECT OBSERVATION OF THE PRIMARY STATE OF DAMAGE OF ION-IRRADIATED TUNGSTEN: I. THREE-DIMENSIONAL SPATIAL DISTRIBUTION OF VACANCIES[†]

by

Ching-Yeu Wei[*], Michael I. Current[**], and David N. Seidman[††]
Cornell University, Bard Hall, Department of Materials
Science and Engineering and the Materials Science Center,
Ithaca, New York 14853, U.S.A.

ABSTRACT

The results of an extensive field-ion microscope (FIM) investigation of the primary state of damage of ion-irradiated tungsten were presented. Two-pass zone-refined single crystals of tungsten were irradiated in situ, at ≤ 15 K, with a magnetically analyzed beam of various ions at a background pressure of $(5-10)x10^{-10}$torr in the absence of the imaging electric field. The value of the standard fluence was small enough ($5x10^{12}cm^{-2}$) to guarantee that each depleted zone (DZ) detected was associated with a single projectile ion. After an irradiation each specimen was examined on an atom-by-atom basis employing the pulse field-evaporation technique. The two main experimental programs were: (1) the determination of the effect of the mass of the projectile ion (M_1) on the three-dimensional spatial distribution of vacancies in DZs, in specimens which had been irradiated with 30 keV W^+, Mo^+, Kr^+, Cu^+, Cr^+, or Ar^+ ions; and (2) the characterization of the effect of the initial energy of the projectile ion (E_1) on the vacancy structure of DZs created by 15, 30, 45, 60 or 70 keV Kr ions. Three-dimensional visualizations were presented of a number of the DZs detected, based on the use of the OR TEP program. The average number of vacancies ($<\nu>$) per DZ was 172 for E_1 = 30 keV, independent of M_1, for the range of ion masses employed. The value of the average vacancy concentration per DZ decreased from ≈ 16 to 2 at.% as M_1 was decreased from 183.85 amu (W) to 39.948 amu (Ar) for E_1 = 30 keV. For the Kr ion irradiations the value of $<\nu>$ increased linearly as E_1 was increased from 15 to 70 keV. Many other detailed physical properties of the DZs were presented in the paper.

[†] This research was supported by the U.S. Department of Energy under Contract No. DE-AS02-76ER03158. Additional support was received from the National Science Foundation through the use of the technical facilities of the Materials Science Center at Cornell University.

[*] Now at General Electric Corporate Research and Development Laboratory, Schenectady, New York 12301.

[**] Now at Signetics Corporation, Sunnyvale, California 94086.

[††] John Simon Guggenheim Memorial Foundation Fellow 1980-81.

§1. INTRODUCTION

The experimental study of the primary state of radiation damage represents an essential test of the theoretical models and descriptions of this subject that have evolved slowly, but steadily, over the past twenty-six plus years (e.g., see Brinkman 1954, Gibson et al. 1960, Seeger 1958, 1962, Nelson 1968, Thompson 1969, Seidman 1976). From the point-of-view of either the experimentalist or theorist one would like to know, in detail, the fate of a single energetic projectile ion that has been injected into solid. The field-ion microscope (FIM) with its excellent atomic resolution and the ability to examine the interior of specimens--as a result of the field-evaporation effect (Müller and Tsong 1969, 1973)--is ideally suited for the study of the three-dimensional spatial distributions of point defects, both vacancies and self-interstitial atoms (SIAs), produced by a single projectile ion (e.g., see Seidman 1973, 1976, 1978, Wei and Seidman 1978, 1979, 1980, Seidman, Current, Pramanik and Wei 1980, Pramanik 1980). The measured three-dimensional spatial distribution of vacancies, for a single projectile ion, is a direct reflection of how the initial energy of that projectile ion was deposited in a series of elastic collisions. Thus the FIM determinations of these spatial distributions represent the most fundamental type of experimental information presently available on the primary state of radiation damage.†

The principle capabilities and advantages of the FIM technique for the study of radiation damage are as follows: (1) The resolution of individual vacancies and self-interstitial atoms; (2) the observation and irradiation of specimens at cryogenic temperatures (≲10 K) which are below the onset of long-range migration of self-interstitial atoms; (3) the *in situ* irradiation of FIM specimens under ultra-high vacuum conditions with a magnetically analyzed ion beam; and (4) the controlled dissection of the FIM specimens on an atom-by-atom basis employing the pulse field-evaporation technique.

---

† In this paper we present results on the spatial distribution of vacancies only. The research on the distribution of SIAs around DZs has been reported on by Beavan et al. (1971) and Wei and Seidman (1980).

The present work represents a major extension (Wei 1978 and Wei and Seidman 1979) of our earlier research on the vacancy structure of depleted zones (DZs)[†] (Beavan, Scanlan and Seidman 1971, Wilson and Seidman 1973, Wei and Seidman 1978). In this paper (Part I) we present the main results of the following experimental programs:

(1) The determination of the effect of the mass of the projectile ion (M_1) on the three-dimensional spatial distribution of vacancies in DZs, in tungsten specimens, which had been ion-irradiated in situ, at ≤ 15 K, at a constant initial projectile energy (E_1) -- the projectiles W^+, Mo^+, Kr^+, Cu^+, Cr^+ and Ar^+ were employed for $E_1 = 30$ keV (see fig. 1); and

(2) The characterization of the effect of E_1, at constant M_1, on the vacancy structure of DZs in tungsten -- 15, 30, 45, 60 or 70 keV Kr ions were employed (see fig. 1).[††]

All of the DZs analyzed were produced at small values of the ion fluence so that each DZ was created by a single projectile ion. A total of eight different physical properties of each DZ were determined (see §3). The main emphases of this paper are on the presentation of the detailed experimental results and a qualitative explanation of the observed trends for the two main experimental programs. The more detailed aspects of this work are presented in two subsequent papers (Current, Wei and Seidman 1980 a, 1980 b). It is emphasized that all of the DZs presented in this paper would not have been observable by conventional transmission electron microscope (TEM) techniques. The TEM technique depends heavily on the ability of the vacancy-rich core of a DZ to collapse into a dislocation loop with sufficient strain-field contrast to make it "visible" in an electron microscope image.[†††] Thus the FIM observations complement the TEM studies of the primary state of damage (e.g., see Eyre 1973, Wilkens 1975, Jenkins 1974, Merkle 1976, Jenkins and Wilkens 1976, Ruault, Bernas and Chaumont 1979).

[†] A depleted zone (DZ) is the end result of a displacement spike or collision cascade (e.g., see Nelson 1968, Thompson 1969). That is, it consists of the final spatial arrangement of the vacancies produced in a displacement spike -- that was created by a single energetic projectile ion -- after all the excess energy deposited in this volume of the crystal has been dissipated.

[††] One data point was obtained for a 45 keV Xe^+ irradiation; it was included for completeness.

[†††] In the TEM work of Jenkins and Wilkens (1976), on ion-irradiated Cu_3Au, the contrast effects produced arose from "the difference in the structure factor between the disordered zone and the ordered matrix". This TEM technique is only applicable to order-disorder alloys.

§2. EXPERIMENTAL DETAILS

2.1. Techniques and procedures

The basic experimental techniques and procedures were presented in detail in a number of earlier publications (for example, Scanlan, Styris and Seidman 1971 a, Seidman and Scanlan 1971, Beavan, Scanlan and Seidman 1971, Wilson and Seidman 1975, Wei and Seidman 1977, 1978, Wei 1978, Current, Wei and Seidman 1980 c). Therefore in this section only the main aspects of the experimental approach are discussed.

The FIM specimens were prepared from two-pass zone-refined single crystals of tungsten by a special electropolishing procedure (Wilson and Seidman 1975). These specimens were then field evaporated to a final end form with an average initial radius of ∿250 Å. Next they were irradiated _in situ_, in the absence of the electric field, with a magnetically analyzed beam of ions at a background pressure of (5-10)x10^{-10} torr. A standard fluence of $5 \times 10^{12} cm^{-2}$ was collected in approximately five minutes employing a flux of $(2\text{-}3) \times 10^{10} cm^{-2} sec^{-1}$; at this value of the flux the time to form an adsorbed monolayer was greater than the irradiation period. After an irradiation the voltage on the specimen was returned immediately to best image field for helium as the imaging gas (Müller and Tsong 1969, Chen and Seidman 1971) in order to prevent the adsorption of gases, from the background vacuum, on the irradiated surface.

The temperature of the specimen was maintained at ≤15 K during and after the irradiation period. At a temperature of ≤15 K we have shown that the SIAs in tungsten were completely immobile; that is, there were no long-range migration effects (Scanlan, Styris and Seidman 1971 a and 1971 b, Seidman, Wilson and Nielsen 1975 a and 1975 b, Wei and Seidman 1979, Wilson, Baskes and Seidman 1980). Thus the observed state of radiation damage was characteristic of the defects produced during the slowing down of the energetic projectile ions and was not altered by any thermally activated long-range migration or recombination processes. In view of these experimental conditions we believe that our observations were characteristic of the primary state of radiation damage (Seidman 1976).[†]

After an irradiation each specimen was dissected, at the irradiation temperature, on an atom-by-atom basis--employing careful pulse field evaporation experiments. Typically ten to 50 voltage pulses were employed to dissect an important {hkl} plane --for example, the {111} planes--and the pulse field-evaporation sequences were recorded on 35 cm ciné film; a total of 6,400 to 19,000 frames of film were recorded per irradiated specimen. Each field-evaporation pulse was 5 msec wide and the height of the pulse was ∿20% of the best image field for helium gas at a specimen temperature of ≤15 K (Chen and Seidman 1971).

The film was analyzed with the aid of a Vanguard motion analyzer equipped with x-y cross-hairs which were interfaced to a Houston Omnigraphic 200 x-y point plotter (Scanlan et al., 1969, Wei 1978). Some of the procedures used to determine the atomic coordinates of the individual vacancies contained within DZs have been reported elsewhere (Wei and Seidman 1978, Wei 1978). In the Appendix the procedure used to analyze a DZ, that extended over several {hkl} planes, was presented. The position of the vacancies contained within each DZ were displayed employing the OR TEP program (Johnson 1965, 1970); for prior applications of this program see Wei and Seidman (1978 and 1979), Current and Seidman (1980), and Current, Wei and Seidman (1980 c).

2.2. The mass and energy of the projectile ions

The values of M_1 and E_1 were chosen in a systematic fashion so that the results could be compared to the available models of the primary state of radiation damage. Figure 1 exhibits the values of E_1 (in keV) as a function of the Linhard, Scharff and Schiøtt (1963) reduced energy parameter (ε); ε proved itself to be a convenient scaling parameter for analyzing our data. The parameter ε is given by

$$\varepsilon \equiv \frac{M_2E_1}{(M_1+M_2)} \Bigg/ \frac{Z_1Z_2e^2}{a_{TF}} , \qquad (1)$$

[†] This paper contains a complete bibliography of all the FIM research on the primary state of damage through 1976.

where M_1, Z_1, M_2 and Z_2 are the masses and atomic numbers for the projectile and target atoms, respectively, e is the charge on an electron and a_{TF} is the Thomas-Fermi screening length. The expression used for a_{TF} was

$$a_{TF} = 0.8853 a_H / \sqrt{Z_1^{2/3} + Z_2^{2/3}} , \qquad (2)$$

where a_H is the Bohr radius (0.529 Å). Equation (1) represents, physically, the ratio of the initial kinetic energy in the center-of-mass frame of reference to the Coulomb repulsion energy evaluated at a_{TF}. Note that the experiments spanned almost one order-of-magnitude in the range of initial values of ε employed ($\sim 1.9\times10^{-2}$ to 1.2×10^{-1}).

§3. RESULTS

3.1. Principal quantities determined

The principal experimental quantities determined from the analyses performed on all the individual DZs observed were as follows:[†]

(1) The direct determination of the absolute number of vacancies (ν) contained within each DZ that was created by a single projectile ion;

(2) Visual representations -- with the aid of the OR TEP program -- of the positions of the vacancies included within every DZ;

(3) The measurement of the average diameter ($\langle\lambda\rangle$) of an individual DZ and the orientation of the DZ with respect to the ion beam and the crystal lattice;

(4) A calculation of the average vacancy concentration ($\langle c_v \rangle$) within each DZ based on ν and the <u>actual</u> volume (Wei 1978) filled by the vacancies;

(5) A calculation of two different types of radial distribution functions (Wei 1978 and Wei and Seidman 1979) for the vacancies comprising each DZ;

(6) The determination of the fraction of first-nearest-neighbor vacancies -- within each DZ -- in clusters of size n, where n ranged from one to several hundred;

[†] See Current, Wei and Seidman (1980 a) for details concerning the definitions of these quantities.

(7) The average depth (L) from the irradiated surface, measured along a direction parallel to the incident ion beam, at which each DZ was detected and the direction of elongation ([hkl]) of each DZ; and

(8) The measurement of the number (ν_{ns}) and concentration ($<c_v>_{ns}$) of vacancies which were found in the near-surface region (<5 Å thick) of ion-irradiated tungsten specimens (Current and Seidman 1980, Current, Wei, and Seidman 1980 c).

In this paper we have presented a number of examples of the OR TEP visualization of DZs. A qualitative discussion of the major properties of the DZs, that were gleaned from these visualizations, was also given. Detailed analyses and discussions of the principal results -- numbers (1) to (7) above -- are presented in the following two papers (Current, Wei and Seidman 1980 a and 1980 b). A comparison of the properties of DZs which contained vacancies in the near-surface region with those DZs which were found in the bulk of FIM specimens was given earlier by Current and Seidman (1980) and Current, Wei and Seidman (1980 c).

§3.2. Examples of depleted zones in tungsten

Results for a total of 39 DZs were reported on in this series of papers (see Tables 1 and 3). Since it was found impossible to present all of the micrographs for all of the DZs we have only exhibited selected FIM micrographs for the pulse dissection of two DZs; for other micrographs see Wei (1978).

Figure 2 exhibits schematically the results for three different 30 keV W^+ ion irradiations of tungsten specimens which had a [211] orientation; the ion beam was initially parallel to the ≃$[\bar{8}\ 11\ 5]$ direction. The cross-sectional side views of the specimen are shown in figs. 2(b), 2(d) and 2(f); the position of each DZ was projected into the plane of this figure. The distances between pairs of DZs are indicated by the letters a,b,c, etcetera; they ranged from

50 to 140 Å. Figures 2(a), 2(c) and 2(e) exhibit the partial 211 standard stereographic projections for the specimens shown in the bottom half of this figure. The plane (or planes) in which a DZ was detected is indicated in the stereographic projection; for example, DZ3a was found in the $(7\bar{1}2)$ and $(8\bar{1}3)$ planes of the third specimen -- see figs. 2(e) and 2(f).

An illustrative example of the contrast effects associated with a DZ that was produced by a single 30 keV W^+ ion is exhibited in fig. 3. This figure shows a series of FIM micrographs of ten successive planes; they were chosen from a total of 1.4×10^3 frames of 35 mm ciné film which were recorded and analyzed in the reconstruction of DZ3a. The $(8\bar{1}3)$ plane and the neighboring planes are indexed in frame 1; the frame number of the ciné film is shown in the lower right-hand corner below each micrograph; and the layer number is given in the upper left-hand corner above each micrograph -- for example, frame number 47 is the n = 2 layer.† The position of each atom in the $(8\bar{1}3)$ plane is indicated schematically below each micrograph by a solid black circle and a vacancy is indicated by an open circle. The ten planes exhibited in fig. 3 contained 50 vacancies out of the total of 242 vacancies detected in this DZ. DZ3a was found at $L\simeq45$ Å and it was elongated along the $[\bar{1}01]$ direction; the values of $\langle\lambda\rangle$ and $\langle c_v\rangle$ for this DZ were 13 Å and 17 at.%, respectively (see Table 1). The vacancies contained within DZ3a were in a highly clustered state. For first-nearest-neighbor vacancies the distribution of cluster sizes was as follows: (1) 28 monovacancies; (2) two divacancies; (3) one quadrivacancy; and (4) one jumbo cluster containing 206 vacancies.

Figure 4 displays pictorially the results of a 30 keV Mo^+ ion irradiation parallel to the $\simeq[8\ \bar{5}\ 11]$ direction of a tungsten specimen with a [211] orientation. Four DZs (DZ4a to DZ4d) plus one dislocation loop were detected in this specimen. A partial 211 stereographic projection, which shows the top view of the specimen,

---

† Note that n is used in a special sense in figs. 3 and 5 which is different from the n used to denote the size of a vacancy cluster.

is shown in fig. 4(a); the corresponding cross-sectional side view is shown in fig. 4(b). The separation between any pair of DZs ranges from 90 to 160 Å.

An illustrative example of the contrast effects produced by a DZ created by a single 30 keV Mo^+ ion is shown in fig. 5; these micrographs are for DZ4b. Figure 5 exhibits a series of ten FIM micrographs for ten successive (622) planes, n = 1 to 10; they were chosen from among 1.0×10^3 frames of 35 mm ciné film recorded and analyzed in the reconstruction of DZ4b. Frame number one shows an atomically perfect (622) plane in the n = 1 layer; the other nine frames display (622) planes containing vacancies. Note that a void-like cluster appeared in the n = 6 to n = 10 layers of the (622) plane and 20 vacancies were detected among 60 lattice sites -- this corresponds to a local vacancy concentration of ∿33 at.%.† Note, however, that the value of $<c_v>$ was 10 at.% for all the vacancies that were contained in DZ4b, which extended over both the (411) and (622) planes. The arrows in frames 76 and 131 pinpoint another void-like cluster observed in the (411) plane. DZ4b was located at L ≃ 40 Å and it was elongated along the $[\bar{1}11]$ direction; the value of $<\lambda>$ was 15 Å. For first-nearest neighbor vacancies the distribution of cluster sizes was as follows: (1) 37 monovacancies; (2) four divacancies; (3) one quadrivacancy; (4) one octavacancy; and (5) two jumbo clusters containing 27 and 76 vacancies. A comparison of the OR TEP visualizations (see §3.3) for DZ3a and DZ4b clearly showed that the latter consisted of two major subcascades.

3.3. OR TEP visualizations of depleted zones created by 30 keV ions

In this section we present examples of OR TEP visualizations of the atomic positions of vacancies contained within individual DZs which had been created by

---

† The (622) plane exhibited an artifact vacancy concentration of 0.8 at.% (Wei and Seidman 1980). However, the observation of this high local concentration associated with the vacancies detected in the (622) plane could not have been due to artifact vacancies.

single 30 keV ions.[†] The projectile ions employed[††] for the irradiations were W(183.85 amu), Mo(95.94 amu), Cu(63.546 amu), Cr(51.996 amu) and Ar(39.948 amu); this corresponded to a factor of 4.60 in the range of M_1 and almost one order of magnitude in the value of ε (see fig. 1). Figure 6 illustrates the general effects observed as M_1 was decreased; this figure contains three different DZs (DZ1a, DZ4b and DZ5a) which were produced by 30 keV W^+, Mo^+, or Cr^+ ions, respectively. Each open circle represents one vacancy, and the rod connecting two vacancies has a length equal to the first-nearest neighbor distance (≈2.74 Å); the perfect lattice was omitted for the sake of clarity. This figure shows immediately that as M_1 was decreased the following occurred: (1) the spatial extent of the DZ increased; (2) the vacancy concentration decreased; (3) the number of isolated monovacancies increased and therefore the number of large first-nearest-neighbor vacancy clusters decreased; and (4) there was a tendency to form subcascades within the DZ -- this was particularly apparent in the case of DZ4b which was found to consist of two distinct subcascades.

Six OR TEP visualizations are now presented in order of decreasing M_1 at constant E_1. Details regarding the other 23 DZs are presented in Table 1, which represents a summary of the major effects of M_1 on the vacancy structure of DZs.

<u>DZ2b (fig. 7)</u>: This DZ was created by a W^+ ion and was detected in the $(6\bar{2}2)$ and $(7\bar{2}3)$ planes -- see figs. 2(c) and 2(d). The incident ion beam was parallel to the $[\bar{8}\ 11\ 5]$ direction and the DZ was elongated along the [001] direction. DZ2b was detected at L ≃ 35 Å and it contained 133 vacancies; the values of $\langle\lambda\rangle$ and $\langle c_v\rangle$ were 9 Å and 26 at.%, respectively (see Table 1). The distribution

---

[†] Employing the same geometric argument as the one used previously (Beavan <u>et al</u>. 1971, Wilson and Seidman 1973, Wei and Seidman 1978) it was estimated that the maximum number of ion hits on the cross-sectional area of each DZ was always less than one. This value was an upper bound because it neglected the straggling in the range of the projectile ion.

[††] We also performed 30 keV Kr^+ irradiations; however, they were intended mainly for the E_1 dependence experiments described in §3.4.

of first-nearest neighbor vacancy clusters was as follows: (1) eleven monovacancies; (2) one divacancy; and (3) one huge cluster containing 120 vacancies. Even at a local value of $<c_v>$ approaching 30 at.% the remaining tungsten atoms still formed a recognizable, although somewhat deformed bcc lattice.

DZ3a (fig. 8): This DZ was detected in the $(7\bar{1}2)$ and $(8\bar{1}3)$ planes -- see figs. 2(e) and 2(f). A partial pulse field-evaporation sequence through DZ3a is exhibited in fig. 3 and we presented values for its principal experimental parameters in §3.2. Note that both this DZ and DZ2b, which were created by 30 keV W^+ ions, were extremely compact and contained very few isolated monovacancies.

DZ4d (fig. 9): This DZ was created by a Mo^+ ion and it was detected in the $(41\bar{1})$, $(71\bar{2})$ and $(51\bar{2})$ planes (see fig. 4). The incident ion beam was parallel to the $[\bar{8}\ 5\ 11]$ direction and the DZ was elongated along the [111] direction. DZ4d was detected at $L \simeq 35$ Å and it contained 169 vacancies; the values of $<\lambda>$ and $<c_v>$ were 15 Å and 9 at.%, respectively. The distribution of first-nearest neighbor vacancy clusters was as follows: (1) 29 monovacancies; (2) six divacancies; (3) one trivacancy; and (4) three large clusters containing 24, 28 and 72 vacancies. The breakup of this DZ into two large subcascades, each of which contained approximately the same number of vacancies, is clear from fig. 9.

DZ6a (fig. 10): This DZ was created by a Cu^+ ion. The incident ion beam was parallel to the $[\bar{1}5\bar{6}]$ direction and the direction of elongation was [110]. DZ6a was detected at $L \simeq 220$ Å and it contained 130 vacancies; the values of $<\lambda>$ and $<c_v>$ were 30 Å and 3.4 at.%, respectively. The distribution of first-nearest neighbor clusters was as follows: (1) 57 monovacancies; (2) four divacancies; (3) one trivacancy; (4) two quadrivacancies; (5) one hexavacancy; (6) two octavacancies; and (7) one large cluster of 32 vacancies.

DZ7a (fig. 11): This DZ was created by a Cu^+ ion. The incident ion beam was parallel to the $[\bar{4}31]$ direction and the DZ was elongated along the [001] direction. DZ7a was detected at $L \simeq 230$ Å and it contained 243 vacancies; the values of $\langle\lambda\rangle$ and $\langle c_v\rangle$ were 27 Å and 3.7 at.%, respectively. The distribution of first-nearest neighbor vacancy clusters was as follows: (1) 70 monovacancies; (2) 15 divacancies; (3) four trivacancies; (4) two hexavacancies; and (5) three large clusters of 15, 22 and 66 vacancies. The breakup of this DZ into three distinct subcascades is very evident from an examination of fig. 11.

DZ5a (fig. 12): This DZ was created by a Cr^+ ion and was detected in five crystallographic planes -- the (512), (723), (824), (411) and (11 3 4) planes. The incident ion beam was parallel to the $[\bar{7}4\bar{1}]$ direction and it was elongated along the $[1\bar{1}0]$ direction. DZ5a was detected at $L \simeq 40$ Å and it contained 245 vacancies; the values of $\langle\lambda\rangle$ and $\langle c_v\rangle$ were 31 Å and 3.6 at.%, respectively. The distribution of first-nearest-neighbor vacancy clusters was as follows: (1) 69 monovacancies; (2) seven divacancies; (3) six trivacancies; (4) one quadrivacancy; (5) three pentavacancies; (6) one hexavacancy; (7) one heptavacancy; (8) one octavacancy; and (9) four large clusters containing 9, 15, 30 and 50 vacancies. Note that although $\langle c_v\rangle$ was 3.7 at.%, that there are several regions within this DZ where the local vacancy concentration was three to five times greater than this average value. Local inhomogeneities in the vacancy concentration was a general feature of the DZs created by lighter projectiles (also see DZ7a in fig. 11).

The degree of clustering within the DZs created by different 30 keV ions was further quantified by calculating the fraction of vacancies in first-nearest-neighbor clusters of size n (F_n). The expression for F_n employed was

$$F_n = nN_n \Big/ \left(\sum_n nN_n\right), \tag{3}$$

where n was the size of the cluster and N_n the number of clusters of size n. The value of the sum in the denominator of eqn. (3) is equal to the measured value of

ν. Table 2 lists the average values of F_n for the DZs created by the various 30 keV ions, including the 30 keV Kr^+ ions. The general trend was that as M_1 decreased the fraction of monovacancies (F_1) increased and concomitantly the fraction of clusters with $n \geq 5$ ($F_{n\geq 5}$) decreased.

3.4. OR TEP visualizations of depleted zones created by krypton ions with energies between 15 to 70 keV

A series of irradiations were performed with Kr ions (83.80 amu) to examine the spatial distribution of vacancies at constant M_1 and varying E_1; the value of E_1 was varied between 15 and 70 keV (see fig. 1). The principal experimental quantities determined for the DZs obtained as a result of these irradiations are listed in Table 3. The OR TEP visualization of five of these DZs are presented in this section to illustrate the changes that occurred in the properties of the DZs as E_1 was increased. The qualitative trends that emerged as E_1 was increased at constant M_1 were as follows: (1) the value of $\langle \nu \rangle$ increased; and (2) the value of $\langle c_v \rangle$ decreased and then increased -- see the results for the 70 keV Kr^+ DZ.

The descriptions of the OR TEP visualizations (figs. 13-16) are as follows:

DZ15b (fig. 13): This DZ was created by a 15 keV Kr^+ ion. The incident ion beam was parallel to the $[\bar{3}\bar{1}4]$ direction and the DZ was elongated along the $[11\bar{1}]$ direction. DZ15b was detected at $L \approx 60$ Å and it contained 109 vacancies; the values of $\langle \lambda \rangle$ and $\langle c_v \rangle$ were 24 Å and 5.7 at.%, respectively. The distribution of first-nearest neighbor vacancy clusters was as follows: (1) 43 monovacancies; (2) three trivacancies; and (3) two large clusters of 15 and 42 vacancies.

DZ14b (fig. 14): This DZ was created by a 30 keV Kr^+ ion. The incident ion beam was parallel to the $[\bar{4}13]$ direction and the DZ was elongated along the [110] direction. DZ14b was detected at $L \approx 60$ Å and it contained 238 vacancies; the values of $\langle \lambda \rangle$ and $\langle c_v \rangle$ were 23 Å and 5.9 at.%, respectively. The distribution of first-nearest neighbor vacancy clusters was as follows: (1) 54 monovacancies; (2) 11 divacancies; (3) six trivacancies; (4) two quadrivacancies; (5) two pentavacancies; (6) one hexavacancy; and (7) three large clusters of 23, 47 and 50 vacancies. Note the similarity of this DZ to DZ4d (fig. 9) -- which was created by a 30 keV Mo^+ ion (95.94 amu) -- and DZ7a (fig. 11) which was created by a 30 keV Cu^+ ion (63 amu).

<u>DZ8a (fig. 15)</u>: This DZ was created by a 45 keV Kr^+ ion. The incident ion beam was parallel to the $[\bar{1}01]$ direction and the DZ was elongated along the [011] direction. DZ8a was detected at L ≃ 240 Å and it contained 298 vacancies; the values of $<\lambda>$ and $<c_v>$ were 32 Å and 4.3 at.%, respectively. The distribution of first-nearest neighbor vacancy clusters was as follows: (1) 47 monovacancies; (2) seven divacancies; (3) one trivacancy; (4) one quadrivacancy; and (5) seven large clusters of 10, 14, 19, 33, 45, 46 and 63 vacancies.

<u>DZ9a (fig. 16)</u>: This DZ was created by a 60 keV Kr^{+2} ion. The incident ion beam was parallel to the $[\bar{5}32]$ direction and the DZ was elongated along the [111] direction. DZ9a was detected at L ≃ 100 Å and it contained 378 vacancies; the values of $<\lambda>$ and $<c_v>$ were 31 Å and 2.7 at.%, respectively. The distribution of first-nearest neighbor vacancy clusters was as follows: (1) 151 monovacancies (2) 29 divacancies; (3) four trivacancies; (4) two quadrivacancies; (5) one pentavacancy; (6) one heptavacancy; (7) one cluster of nine vacancies; and (8) a jumbo cluster of 128 vacancies.

<u>DZ13a (fig. 17)</u>: This DZ was created by a 70 keV Kr^{+2} ion. The incident ion beam was parallel to the $[\bar{1}2\bar{1}]$ direction and the DZ was elongated along the $[10\bar{1}]$ direction. DZ13a was detected at L ≃ 170 Å and it contained 378 vacancies; the values of $<\lambda>$ and $<c_v>$ were 16 Å and 12.3 at.%, respectively. The distribution of first-nearest neighbor vacancy clusters was as follows: (1) 62 monovacancies; (2) 14 divacancies; (3) four trivacancies; (4) two quadrivacancies; (5) one heptavacancy; (6) one octavacancy; and (7) a jumbo cluster of 253 vacancies. The

highly compact nature of this DZ was consistent with observations of DZs created by 60 keV W^+ ions in tungsten (Pramanik 1980). This very concentrated vacancy distribution is relevant to the problem of the mechanism of collapse of a DZ into a dislocation loop.

§4. DISCUSSION

The results presented in §3 constitute the experimental analog of individual displacement cascades which have been simulated employing either the Monte Carlo (e.g., Beeler 1966 and Robinson and Torrens 1974) or molecular dynamics (Gibson et al. 1960) computer techniques. The reason for this is that each DZ was created by a single projectile ion. Hence, the distribution of vacancies within each DZ represents a direct reflection of how the energy of a single projectile ion was deposited in a series of elastic collisions. This direct measurement of ν, for each DZ, constituted as close as anyone has come to achieving a simple Frenkelometer that determines an absolute value of ν.

Before discussing the results we review briefly some elementary theoretical concepts that are relevant to this work. Figure 18 is a plot of the reduced stopping power $[S(\varepsilon)]$ as a function of ε. The total stopping power of the target for a projectile ion is generally taken to be the sum of the elastic (or nuclear) stopping power (S_n) plus the inelastic (or electronic) stopping power (S_e) [Linhard, Scharff and Schiøtt (LSS) 1963]. When E_1 is expressed in terms of ε the plot of $S_n(\varepsilon)$ as a function of ε is a universal curve for all combinations of projectiles and targets $(\bar{Z}_1, \bar{M}_1; \bar{Z}_2, M_2)$ and a given interatomic potential. The quantity $S_n(\varepsilon)$ is given by the expression

$$S_n(\varepsilon) = -\left(\frac{d\varepsilon}{d\rho}\right) ; \qquad (4)$$

where ρ is the dimensionless distance

$$\rho = \pi a_{TF}^2 [4M_1M_2/(M_1+M_2)^2] N_dR; \tag{5}$$

N_d is the number density of atoms in the target and R is the total path length of the projectile in the target. The curves labeled $S_n(\varepsilon)$ are for a Thomas-Fermi interatomic potential (Linhard, Scharff and Schiøtt 1963) and a Moliére-like potential [Wilson, Haggmark and Biersack (WHB) 1977], respectively. The Linhard-Scharff (1961) expression for S_e is given by

$$S_e = K\varepsilon^{1/2} , \tag{6}$$

where

$$K = \frac{0.0793Z_1^{2/3}Z_2^{1/2}(M_1 + M_2)^{3/2}}{(Z_1^{2/3} + Z_2^{2/3})^{3/4}M_1^{3/2}M_2^{1/2}} , \tag{7}$$

was used to calculate S_e for the cases of W^+ and Cr^+ ions on tungsten; note that the value of S_e, at a given ε, depends on the particular combination of projectile and target atoms and, therefore, there is not a universal curve for $S_e(\varepsilon)$. For the values of E_1 (or ε) employed in our experiments the value of S_n was always greater than the value of S_e for both the LSS and WHB interatomic potentials (see fig. 18). Thus approximately 75%, on the average, of each projectile's energy went into elastic collisions; it was this elastically transferred energy that produced point defects.

Winterbon, Sigmund and Sanders (1970) suggested for the case of $\varepsilon \leq 0.2$ that S_n(LSS) can be approximated† by

$$S_n = 0.98\varepsilon^{1/3} , \tag{8}$$

---

† These expressions were calculated for a stopping cross-section that has an interatomic potential of the form $V(r) \propto r^{-3}$, where r is the internuclear separation. For values of $\varepsilon \lesssim 10^{-2}$ these expressions are not expected to be valid (Linhard et al. 1963 and Wilson et al. 1977). However, we have presented them because they represent simple first-order expressions for very important quantities.

to an accuracy of ∿20%. These authors also suggested that the corresponding approximate expression for $\rho(\varepsilon)$ in this régime is

$$\rho(\varepsilon) = 1.53\varepsilon^{2/3}. \tag{9}$$

For the range of M_1 and ε involved in the present experiments the values of R and the projected range are approximately the same (Linhard, Scharff and Schiøtt 1963); therefore, we can take the volume of the displacement cascade $[\omega(\varepsilon)]$ to be given by Sigmund (1974, 1975, 1980)

$$\omega(\varepsilon) \sim \text{constant}\ [\rho(\varepsilon)]^3 \propto \varepsilon^2; \tag{10}$$

where $\rho(\varepsilon)$ is assumed to be the projected range of the projectile ion. Physically eqn. (10) states that $\omega(\varepsilon)$ is proportional to the third power of $\rho(\varepsilon)$. It is not obvious that the radius of a single displacement cascade should always be proportional to $\rho(\varepsilon)$, thus the dependence predicted by eqn. (10) may not be generally correct (Sigmund 1980).

4.1. Depleted zones created by 30 keV ions

The experimental variation of ν with M_1 was not very strong (see Table 1). The reason for this important result rests with the fact that S_e varied weakly with M_1 (see fig. 18) for the range of values of M_1 employed. Thus, to first order, ν was independent of M_1 and $\langle\nu\rangle$ was equal to 172 vacancies. This value was in good agreement with the well-known Kinchin-Pease (1955) expression as modified by Robinson and Torrens (1974). The quantity $\langle\nu\rangle$ is considered in more detail in Parts II and III. However, we emphasize very strongly that the spatial distribution of vacancies within a given DZ was a very strong function of M_1, as pointed out in §3.3 (see figs. 6-12 and Table 1).

The reasons for the latter observation can be understood from the following qualitative discussion, which is based on an elastic hard sphere model. First, the maximum energy which can be transferred to a lattice atom in an elastic binary collision (T_{max}) is given by

$$T_{max} = 4M_1M_2(M_1 + M_2)^{-2}E_1 = \gamma E_1; \qquad (11)$$

thus, T_{max} decreased as M_1 was decreased. Also, the mean free path between collisions that involved the transfer of large energies (λ^*) increased as M_1 was decreased. This conclusion was based on the fact that λ^* is inversely proportional to the total elastic cross-section (σ_{total}) for an energy transfer with a given impact parameter and σ_{total} decreases as M_1 is decreased at a constant E_1 (Winterbon, Sigmund and Sanders 1970). Similarly, the quantities involving length increased as M_1 was decreased; that is, $R(E_1)$ and $\rho(\varepsilon)$ (see Winterbon et al. 1970). Hence, an approximately constant number of vacancies was produced in a volume that grew as M_1 was decreased -- see eqn. (10). This implied that $<c_v>$ must decrease as M_1 was decreased. And, indeed, this was the situation observed.

The change in the degree of clustering within the DZs created by the different 30 keV projectiles can also be understood qualitatively on the basis of the variation of λ^* with M_1. For a self-ion irradiation ($M_1 = M_2$) the values of λ^* were so small that the different recoil branches of each displacement cascade were highly localized in space, thus there was a very high probability that many of the branches overlapped one another. As M_1 was decreased λ^* increased and the probability of overlap decreased. The above qualitative physical description is illustrated in fig. 19 for W^+, Mo^+ and Cr^+ projectiles impinging on a tungsten target. The angle between the deflected projectile atom and recoiling target atom ($\theta_1 + \theta_2$) was calculated under the assumption that the transferred energy (E_2) was given by

$$E_2 = 0.5T_{max} = 0.5\gamma E_1 \ . \tag{12}$$

Thus the recoil angle in the center-of-mass frame of reference (ϕ) was 90°, independent of the value of M_1. The angle through which the projectile atom was deflected in the laboratory frame-of-reference (θ_1) is given by

$$\tan\theta_1 = \sin\phi/[\cos\phi + (M_1/M_2)]; \tag{13}$$

therefore, θ_1 is equal to 45°, 62.44° and 74.21° for W, Mo and Cr on tungsten, respectively. The recoil angle of the target atom in the laboratory frame-of-reference (θ_2) is given by

$$\tan\theta_2 = \sin\phi/(1-\cos\phi) \ . \tag{14}$$

Equation (14) predicts that θ_2 is equal to 45° independent of the mass ratio M_1/M_2. Thus the angle ($\theta_1 + \theta_2$) is equal to 90°, 107.44° and 119.21° for W, Mo and Cr impinging on tungsten, respectively. The increasing value of ($\theta_1 + \theta_2$) implied that the target and projectile atoms were more effectively separated from one another as M_1 was decreased. In addition, the value of T_{max} concomitantly decreased so that the number of vacancies produced per major recoil branch also decreased. This implied that a larger number of elastic collisions was required for the projectile to give up all its initial energy; therefore, the total number of major recoil branches increased as M_1 was decreased at constant E_1. Figure 19 exhibits schematically all of the physical features discussed above.

4.2. Depleted zones created by 15 to 70 keV Kr^+ ions

The main experimental results for the 15 to 70 keV Kr^+ irradiations are summarized in §3.2 and Table 3 and they can be understood qualitatively on the basis of the ideas presented earlier in this section. However, there are problems in understanding all of the details of these observations based solely on the physical picture outlined in the preface to §4.

First, the value of $<\nu>$ was linearly proportional to E_1 (or ε); this was expected on the basis of either a Kinchin-Pease model (1955) or a Robinson-Torrens (1974) type model. Second, the average value of L increased as E_1 (or ε) was increased -- see Table 3. Equation (9) predicted that the projected range $[\rho(\varepsilon)]$ is proportional to $\varepsilon^{2/3}$ for the present ε régime; thus, the observed increase in L with increasing E_1 (or ε) was also expected. Third, the values of $<\lambda>$ also increased with increasing E_1 (or ε), -- with the exception of the DZ created by the 70 keV Kr^+ ion. This result is consistent with the idea that $<\lambda>$ is proportional to $\rho(\varepsilon)$ and therefore $<\lambda>$ is proportional to ε. Fourth, the value of $<c_v>$ decreased with increasing E_1 (or ε) -- with the exception of the DZ created by the 70 keV Kr^+ ion. This last result is in agreement with the concept that $<c_v>$ is proportional to $<\nu>/\omega(\varepsilon)$ and hence to ε^{-1}.

The major inconsistency observed, that went against the predicted trends, was for the one DZ produced by a 70 keV Kr^+ ion. For this case $<\lambda>$ was smaller than the values of $<\lambda>$ observed at all the lower energies. In other work, in our laboratory, Pramanik (1980) found that for self-ion irradiation of tungsten the fraction of aggregate defects[†] that were dislocation loops increased with increasing E_1. Thus, DZ13a may have been frozen-in in a state that was on the verge of collapsing into a platelet or dislocation loop. This point is discussed further in Part III (Current, Wei and Seidman 1980 b).

[†] This term includes: (1) compact vacancy clusters or voids; (2) depleted zones and (3) platelets or dislocation loops; see Seidman (1976) for a discussion of this classification.

§5. SUMMARY

The most important results and conclusions are as follows:

(1) To first order the value of the number of vacancies (ν) contained within each DZ, created by a single projectile ion, was independent of the mass of the projectile ion (M_1) for the case of 30 keV W^+, Mo^+, Kr^+, Cu^+, Cr^+ or Ar^+ ions on tungsten;

(2) The value of $\langle\nu\rangle$ was 172 for an initial projectile energy (E_1) of 30 keV and the ions listed above in (1);

(3) The value of $\langle\nu\rangle$ of 172 was in good agreement with the Kinchin-Pease (1955) expression as modified by Robinson and Torrens (1974) -- see §3.1 in Part II;

(4) The average diameter ($\langle\lambda\rangle$) of the DZs increased as M_1 was decreased at a constant E_1 of 30 keV;

(5) The value of the average vacancy concentration $\langle c_v\rangle$ of a DZ decreased from ≈16 to 2 at.% as M_1 was decreased from 183.85 amu (W) to 39.948 amu (Ar) at a constant E_1 of 30 keV;

(6) The spatial arrangement of vacancies within the DZs was a strong function of M_1 at a constant E_1 of 30 keV -- in general, the number of subcascades within each DZ increased as M_1 was decreased;

(7) The fraction of monovacancies contained within each DZ increased as M_1 was decreased -- at a constant E_1 of 30 keV -- and concomitantly the fraction of vacancies contained within large clusters decreased (see Table 2);

(8) For the Kr ion irradiations the value of $\langle\nu\rangle$ increased linearly as E_1 was increased from 15 to 70 keV;

(9) The value of $\langle\lambda\rangle$ increased as E_1 was increased from 15 to 60 keV for the Kr ion irradiations;

(10) The value of $\langle c_v\rangle$ decreased as E_1 was increased from 15 to 60 keV for the Kr ion irradiations;

(11) For the case of the 70 keV Kr ion irradiation the value of $\langle\lambda\rangle$ was smaller and therefore the value of $\langle c_v\rangle$ was greater than the values observed at all the lower energies; and

(12) It was suggested that the DZ observed in the case of the 70 keV ion irradiation may have been frozen-in in a state that was on the verge of collapsing into a platelet or dislocation loop.

ACKNOWLEDGEMENTS

We thank Mr. R. Whitmarsh for continued enthusiastic technical assistance, S. Rumsey for her help with the OR TEP program, Dr. D. Pramanik for useful discussions, and Mrs. K. Pratt, Mrs. E. Roebig and Ms. B. Wrona for their very careful work on the frame-by-frame analysis of the ciné film.

REFERENCES

Beeler, J.R., 1966, Phys. Rev., 150, 470.

Beavan, L.A., Scanlan, R.M., and Seidman, D.N., 1971, Acta metall., 19, 1339.

Brinkman, J.A., 1954, J. Appl. Phys., 25, 961.

Chen, C.G., and Balluffi, R.W., 1975 a, Acta metall., 23, 919; 1975 b, 23, 931.

Chen, Y.-C., and Seidman, D.N., 1971, Surface Sci., 27, 231.

Current, M.I., and Seidman, D.N., 1980, Nuc. Instrum. Meth., 170, 377.

Current, M.I., Wei, C.-Y., and Seidman, D.N., 1980 a, Cornell Materials Science Center Report No. 4309; 1980 b, Cornell Materials Science Center Report No. ; 1980 c, Cornell Materials Science Center Report No. 4193, accepted for publication in the Philosophical Magazine.

Eyre, B.L., 1973, J. Phys. F: Metal Phys., 3, 422.

Gibson, J.B., Goland, A.N., Milgram, M., and Vineyard, G.H., 1960, Phys. Rev., 120, 1229.

Jenkins, M.L., 1974, Phil. Mag., 29, 813.

Jenkins, M.L., and Wilkens, M., 1976, Phil. Mag., 34, 1155.

Johnson, C.K., 1965, 1970, Oak Ridge National Laboratory (U.S.A.), Report No. 3794 plus revisions.

Kinchin, G.H., and Pease, R.S., 1955, Rep. Prog. Phys., 18, 1.

Linhard, J., and Scharff, M., 1961, Phys. Rev., 124, 128.

Linhard, J., Scharff, M., and Schiøtt, H. E., 1963, Kgl. Danske Videnskab. Selskab., Mat.-Fys. Medd., 33, no. 14.

Merkle, K., 1976, in Radiation Damage in Metals, edited by N.L. Peterson and S.D. Harkness, (Metals Park, Ohio: American Society for Metals), Chapt. 3.

Müller, E.W. and T.-T. Tsong, 1969, Field Ion Microscopy (New York: American Elsevier), Chapt. III and pp. 40-48; 1973, in Progress in Surface Science, edited by S.G. Davison, (Oxford: Pergamon), 81-101.

Nelson, R.S., 1968, The Observation of Atomic Collisions in Crystalline Solids (Amsterdam: North-Holland), Chapt. 5.

Pramanik, D., 1980, Ph.D. Thesis, Cornell University, Ithaca, New York.

Robinson, M.T., and Torrens, I.M., 1974, Phys. Rev. B, 9, 5008.

Ruault, M.O., Bernas, H. and Chaumont, J., 1979, Phil. Mag. A, 39, 757.

Scanlan, R.M., Styris, D.L., and Seidman, D.N., 1971 a, Phil. Mag., 23, 1439; 1971 b, Phil. Mag., 23, 1459.

Scanlan, R.M., Styris, D.L., Seidman, D.N., and Ast, D.G., 1969, Cornell University Materials Science Center Report No. 1159.

Seeger, A., 1958, Proc. 2nd UN Int. Conf. Peaceful Uses of Atomic Energy, Geneva, Vol. 6, p. 250; 1962, Radiation Damage in Solids, (Vienna: IAEA), Vol. I, p. 101.

Seidman, D.N., 1973, J. Phys. F: Metal Phys., 3, 393; 1976, in Radiation Damage in Metals, edited by N.L. Peterson and S.D. Harkness, (Metals Park, Ohio: American Society for Metals), pp. 28-54; 1978, Surf. Science, 70, 532.

Seidman, D.N., Current, M.I., Pramanik, D., Wei, C.-Y., 1980, Cornell Materials Science Center Report No. 4278, accepted for publication in Nucl. Instrum. and Methods (1980).

Seidman, D.N., and Scanlan, R.M., 1971, Phil. Mag., 23, 1429.

Seidman, D.N., Wilson, K.L., and Nielsen, C.H., 1975 a, Phys. Rev. Lett., 35, 1041; 1975 b, in Fundamental Aspects of Radiation Damage in Metals, edited by M.T. Robinson and F.W. Young, Jr., (Springfield, Virginia: National Technical Information Service), Vol. I, pp. 373-396.

Sigmund, P., 1974, Appl. Phys. Lett., 25, 169; 1975, Appl. Phys. Lett., 27, 52; 1980, to appear in Sputtering by Ion Bombardment, edited by R. Behrisch (Berlin: Springer), Chapt. 2.

Thompson, M.W., 1969, Defects and Radiation Damage in Metals (Cambridge, England: Cambridge Press), Chapt. 5.

Wei, C.-Y., 1978, Ph.D. Thesis, Cornell University, Ithaca, New York.

Wei, C.-Y., and Seidman, D.N., 1977, Radiat. Effects, 32, 229; 1978, Phil. Mag. A, 37, 257; 1979, Appl. Phys. Lett., 34, 622; 1980, Cornell Materials Science Center Report No. 4088, accepted for publication in the Philosophical Magazine.

Wilkens, M., 1975, in *Fundamental Aspects of Radiation Damage in Metals*, edited by M.T. Robinson and F.W. Young, Jr., (Springfield, Virginia: National Technical Information Service), Vol. I, pp. 98-112.

Wilson, K.L., and Seidman, D.N., 1973, in *Defects and Defect Clusters in B.C.C. Metals and Their Alloys, Nuclear Metallurgy*, edited by R.J. Arsenault, (College Park, Maryland, University of Maryland), Vol. 18, pp. 216-239; 1975, Rad. Effects, 27, 67.

Wilson, D.L., Baskes, M.I., and Seidman, D.N., 1980, Acta. metall., 28, 89.

Wilson, W.D., Haggmark, L.G., and Biersack, J.P., 1977, Phys. Rev. B, 15, 2458.

Winterbon, K.B., Sigmund, P., and Sanders, J.B., 1970, Kgl. Danske Videnskab. Selskab., Mat.-Fys. Medd., 37, no. 14.

APPENDIX

PROCEDURE FOR THE CONSTRUCTION OF A DEPLETED ZONE WHICH EXTENDED OVER MORE THAN ONE {hkl} PLANE.

In this appendix the procedure employed to construct a DZ in three dimensions from the FIM micrographs is described in detail. The positions of the vacancies found within the specimens were determined employing a Vanguard motion analyzer equipped with x-y crosshairs and interfaced to a Houston Omnigraphic 200 x-y recorder (Scanlan et al. 1969, Wei 1978). The relative coordinates of the vacancies were first recorded in terms of a local coordinate system determined by the unit cell vectors within a given {hkl} plane in which the defects were found (Wei and Seidman 1978). As many of the DZs extended over more than one {hkl} plane, a procedure was developed to mesh the results from neighboring {hkl} planes into a common cubic coordinate system based on the principal directions of the tungsten lattice. The procedure is described below, in step-by-step form for a specific case, to illustrate the principles involved.

(1) The FIM micrograph was first indexed for those {hkl} planes in which a DZ was found. The Miller indices of the vectors which laid along the intersection of any two neighboring {hkl} planes were also calculated. The Miller indices of the planes and the vectors determined on the micrograph were then compared with the schematic diagrams of these planes.

(2) The positions of all the atoms and vacancies in each layer of each {hkl} plane were transferred to a sheet of graph paper with the aid of the x-y cross-hairs on the motion analyzer in conjunction with the x-y recorder. The positions of atoms and vacancies were plotted with respect to one of the common fiducial marks which had been engraved in the phosphor screen portion of the internal image-

intensification system (Wei 1978). The choice of a common reference point[†] eliminated all errors in the positions of atoms caused by the slippage of film in either the ciné camera or the motion analyzer.

(3) Now consider the upper portion of the diagram in fig. 20 which shows the positions of the atoms in two successive layers of the (222) plane. The atomic sites in the zeroth and the first layers are represented by solid black circles and open circles, respectively. The atomic site 0 was chosen arbitrarily as the origin for the zeroth layer. The vector $a_o[\bar{1}10]$ (a_o is the lattice parameter of tungsten) which lies along the intersection of the (222) and (332) planes and the vector $a_o[0\bar{1}1]$ which lies along the intersection of the (222) and (233) planes, as determined in step (1), were taken as the u- and v- axes, respectively. The vector $(a_o/6)[111]$ which is normal to the (222) plane was taken as the Z-axis. This local coordinate system consisting of the u-, v- and Z-axes and point 0 as the origin was then used to specify the positions of any atomic site in the zeroth layer of the (222) plane in terms of integers; for example, the sites 0, A and B have coordinates (0,0,0), (1,0,0) and (0,1,0), respectively.

The atomic site in the first layer which projected within the primitive unit cell of the zeroth layer was denoted by $0'$. The point $0'_p$ denotes the projection of $0'$ onto the zeroth layer. The coordinates of any atomic site in the first layer was determined by using the local coordinate system which consists of the

---

[†] In general two reference points are required to correct errors in the positions of the atoms caused by the two-dimensional slippage of film. In practice, it was found that only one reference point was required in order to correct the errors in the positions of the atoms; this implied that the slippage of the film was essentially one dimensional.

u-, v-, Z-axes and point O'_p as the origin[†]. For example, the site C has the coordinates of (-2, -1, -1) by noting that $\overrightarrow{O'_pC} = \overrightarrow{O'_pO'} + \overrightarrow{O'C} = [00\bar{1}] + [\bar{2}\bar{1}0] = [\bar{2}\bar{1}\bar{1}]$.

The coordinates of any atomic site in any layer of other {hkl} planes were determined in a similar manner. In the lower half of fig. 20, for example, the sites D and E in the zeroth layer of the (332) plane have the coordinates (0,1,0) and (1,0,0) respectively; they were described in the local coordinate system consisting of the vector $a_o[\bar{1}10]$ as the u′-axis, the vector $a_o[\bar{1}\bar{1}3]$ as the v′-axis, $(a_o/22)[332]$ as the Z′-axis and the atomic site O'' as the origin. Similarly, the site F in the first layer of the (332) plane has the coordinates of (1,0,-1) which were described in the same local coordinate system as sites D and E but with O'''_p as its origin. The point O'''_p is the projection of the atomic site O''' onto the zeroth layer. The site O''' in the first layer of the (332) plane projected within the primitive unit cell of the zeroth layer. The use of the local coordinate system for each layer of each (hkl) plane had the advantage that the coordinates of all atomic sites were given by the integers.

(4) Now we consider the problem of the transformation from the local coordinate systems to a common cubic coordinate system. The coordinates of the atomic site C relative to the origin O were obtained by adding the shift vector $\overrightarrow{OO'_p} \equiv \vec{t} = [t_u t_v 0]$ to $\overrightarrow{O'_pC}$. That is, $\overrightarrow{OC} = \overrightarrow{OO'_p} + \overrightarrow{O'_pC} = [t_u t_v 0] + [\bar{2}\bar{1}\bar{1}] = [t_u-2\ t_v-1\ \bar{1}]$. The shift vector $\vec{t}$ is the projection of $\overrightarrow{OO'}$ onto the (222) plane and is given by [0.333333 0.666667 0] (see Table 4). Hence, the site C has the coordinates of (-1.66667, -0.333333, -1) relative to the origin O. In a similar manner the site F has the coordinates of (1.5, 0.727272, -1) relative to the origin O'' by noting that $\overrightarrow{O''F} = \overrightarrow{O''O''_p} + \overrightarrow{O''_pF} = [0.5\ 0.727272\ 0] + [10\bar{1}] =$

[†] The choice of the point O'_p instead of any atomic site, such as Q, as the origin for the first layer of the (222) plane eliminated the accurate measurement of $\vec{OQ}$ as required in the approach used by Chen and Balluffi (1975 a, 1975 b). The benefit of this choice is clear if one notes that $|\overrightarrow{OO'_p}|$ is equal to the magnitude of the shift vector as defined in step (4).

$[1.5\ 0.727272\ \bar{1}]$. The vector $\overrightarrow{O''O''_p}$ given by $[0.5\ 0.727272\ 0]$ (see Table 4) is the shift vector for the (332) plane. The coordinates of any other atomic site in other layers of the planes were determined in the manner described above.

(5) The coordinates of the atomic sites observed in the (222) plane were then transformed to a local cubic coordinate system with O as its origin while those observed in the (332) plane were transformed to another local cubic coordinate system with O'' as its origin. It is noted that the two local cubic coordinate systems are related only by a simple translation vector.

(6) Finally, we have to mesh the two local cubic coordinate systems. In order to transform the coordinates of an atomic site in the local cubic coordinate system of the (332) plane to the local cubic coordinate system of the (222) plane the coordinates of one[†] atomic site R[††], which lies at the intersection of the (222) and (332) planes, were determined according to steps (3) to (5). The coordinates of the atomic site R in the local cubic coordinate system of the (222) plane was denoted by (ξ', ζ', η') and in the (332) plane by (ξ, ζ, η). The coordinates (x, y, z) of an atomic site in the local coordinate system of the (332) plane were finally transformed to the coordinates (x', y', z') in the local cubic coordinate system of

$$x' = x - \xi + \xi' \ ; \qquad \text{(A1)}$$

$$y' = y - \zeta + \zeta'; \qquad \text{(A2)}$$

and

$$z' = z - \eta + \eta'. \qquad \text{(A3)}$$

[†] Since the two local cubic coordinate systems are related only by a translation vector, only one atomic site is needed in determining the transformation equations of the two coordinate systems. In practice, two atomic sites were used; the first atomic site was used to solve the eqns. (A1) to (A3) and the second atomic site was used to check the solutions.

[††] The letter R is used in a special sense in this Appendix and should not be confused with the R defined by eqn. (5).

By extending this procedure all atomic sites observed in all {hkl} planes can be transformed to a common cubic coordinate system. In practice, the computations in steps (4) to (6) were programmed in the language called BASIC and executed with the aid of a Data General Nova 1220 minicomputer in conjunction with a Tetronix 4010 graphic display terminal (see Wei 1978 for details).

Table 1: The effect of the mass of the projectile ion (M_1) on the principal experimental quantities determined.

Projectile ion (M_1)	Initial ion energy (E_1) in keV	Name of depleted zone (DZ)	Number of vacancies per DZ (ν)	Depth of DZ from irradiated surface (L) in Å	Average diameter ($\langle\lambda\rangle$) of a DZ in Å	Direction of elongation [hkl]	Average vacancy concentration $\langle c_v \rangle$ in at.%
W†	20	0a	160	33	15	[110]	14.3
W†	20	0b	81	19	11	$[10\bar{1}]$	13.9
W	30	1a	159	85	11	[110]	27
W	30	1b	121	50	11	[111]	18
W	30	1c	---	20	--	---	---
W	30	2a	141	40	16	$[10\bar{1}]$	13
W	30	2b	133	35	9	[001]	26
W	30	2c	123	10	14	[011]	9
W	30	3a	242	45	13	$[\bar{1}01]$	17
W	30	3b	127	15	22	[010]	4.4
Mo	30	4a	216	50	15	$[\bar{1}01]$	10
Mo	30	4b	160	40	15	$[\bar{1}11]$	10
Mo	30	4c	156	25	19	[011]	11
Mo	30	4d	168	35	15	[111]	9
Mo	30	loop	---	60	--	---	---
Cu	30	6a	130	220	30	[110]	3.4
Cu	30	6b	---	30	--	---	---
Cu	30	7a	243	230	27	[001]	3.7
Cu	30	7b	200	20	25	[100]	5.5
Cu	30	7c	144	10	26	$[\bar{1}11]$	4.6
Cu	30	7d	160	100	49	[100]	1.1
Cu	30	7e	---	30	--	---	---
Cr	30	9a	241	40	31	$[1\bar{1}0]$	3.6
Cr	30	9b	247	60	24	[110]	4.6
Cr	30	9c	---	10	--	---	---
Cr	30	9d	---	106	--	---	---
Cr	30	9e	---	40	--	---	---
Ar	30	10a	192	25	38	$[1\bar{1}1]$	1.8
Ar	30	10b	---	25	--	---	---

† DZ0a and DZ0b were first reported on by Beavan *et al.*; they were reanalyzed in the present work and reported on for completeness.

Table 2: Fraction of vacancies in first-nearest neighbor clusters of size n for E_1 = 30 keV

M_1 \ n	1	2	3	4	≥5
W	0.20	0.05	0.02	0.01	0.72
Mo	0.21	0.07	0.04	0.01	0.66
Kr	0.28	0.12	0.06	0.02	0.52
Cu	0.42	0.11	0.07	0.06	0.33
Cr	0.29	0.06	0.06	0.05	0.54
Ar	0.47	0.12	0.05	0.00	0.36

Table 3: The effect of the initial energy (E_1) of the projectile ion on the principal quantities determined.

Projectile ion (M_1)	Initial ion energy (E_1) in keV	Name of depleted zone (DZ)	Number of vacancies per DZ (ν)	Depth of DZ from irradiated surface (L) in Å	Average diameter ($\langle\lambda\rangle$) of a DZ in Å	Direction of elongation [hkl]	Average vacancy concentration $\langle c_v\rangle$ in at.%
Xe†	45	12a	169	50	31	[001]	2.1
Kr	15	15a	117	90	21	[$11\bar{1}$]	5.8
Kr	15	15b	109	60	24	[$11\bar{1}$]	5.7
Kr	30	14a	103	10	19	[$1\bar{1}0$]	5.5
Kr	30	14b	238	60	23	[110]	5.9
Kr	30	14c	---	110	--	---	---
Kr	45	8a	298	240	32	[011]	4.3
Kr	60	9a	378	100	31	[$\bar{1}11$]	2.7
Kr	60	9b	398	120	27	[$10\bar{1}$]	3
Kr	70	13a	378	170	16	[$10\bar{1}$]	12.3

† This was the only example obtained of a DZ created by an xenon ion. We include this result for completeness.

Table 4: Table of parameters pertinent to the local coordinate system and translation vectors for a number of planes in the bcc lattice

Plane	$\vec{u}^{\dagger}$	$\vec{v}^{\dagger}$	$\vec{Z}^{\dagger}$	$t_u^{\dagger\dagger}$	$t_v^{\dagger\dagger}$
(222)	$[\bar{2}20]$	$[0\bar{2}2]$	[111]	0.333333	0.666667
(332)	$[\bar{2}20]$	$[\bar{1}\bar{1}3]$	[664]	0.500000	0.727272
(433)	$[0\bar{2}2]$	$[3\bar{1}\bar{3}]$	[866]	0.794118	0.411765
(442)	$[\bar{2}20]$	$[0\bar{2}4]$	[442]	0.388888	0.777777
(543)	$[3\bar{3}\bar{1}]$	$[11\bar{3}]$	[10 8 6]	0.340000	0.180000
(875)	$[\bar{1}\bar{1}3]$	$[5\bar{5}\bar{1}]$	[16 14 10]	0.891304	0.601449
(765)	$[3\bar{1}\bar{3}]$	$[\bar{2}4\bar{2}]$	[14 12 10]	0.672727	0.445455
(411)	$[\bar{1}31]$	$[0\bar{2}2]$	[822]	0.555556	0.277778
(521)	$[1\bar{1}\bar{3}]$	$[\bar{1}3\bar{1}]$	[10 4 2]	0.566666	0.233333
(622)	$[02\bar{2}]$	$[\bar{2}24]$	[311]	0.181818	0.363636
(732)	$[\bar{1}3\bar{1}]$	$[\bar{2}24]$	[14 6 4]	0.161290	0.306452
(721)	$[1\bar{3}\bar{1}]$	$[02\bar{4}]$	[14 4 2]	0.259259	0.425926
(631)	$[1\bar{1}\bar{3}]$	$[\bar{1}3\bar{3}]$	[12 6 2]	0.456522	0.195652
(824)	$[2\bar{4}\bar{2}]$	$[04\bar{2}]$	[824]	0.595238	0.857143
(831)	$[1\bar{3}1]$	$[1\bar{1}\bar{5}]$	[16 6 2]	0.851351	0.364865
(11 4 3)	$[2\bar{4}\bar{2}]$	$[11\bar{5}]$	[22 8 6]	0.349316	0.452054

---

† The Miller indices for the $\vec{u}$-, $\vec{v}$- and $\vec{Z}$-axes are given such that the magnitudes of the vectors $\vec{u}$, $\vec{v}$ and $\vec{Z}$ are in units of $a_o/2$, where a_o is the lattice parameter of the standard non-primitive unit cell.

††The values of the quantities t_u and t_v are given in fractions of the magnitudes of the vectors $\vec{u}$ and $\vec{v}$, respectively.

FIGURE CAPTIONS

Figure 1: The initial energy of the projectile ion (E_1) as a function of the Linhard-Scharff-Schiøtt reduced energy parameter (ε); see §2.2 for the definition of ε. The straight lines indicate the experimental conditions employed (see §§1 and 2.2).

Figure 2: (a), (c) and (e) The partial 211 stereographic projections showing the locations of the depleted zones detected for three different 30 keV W^+ ion irradiations parallel to the $\doteqdot[\bar{8}\ 11\ 5]$ direction. (b), (d) and (f) The corresponding cross-sectional views of the FIM tips.

Figure 3: A series of ten micrographs out of 713 recorded during the atom-by-atom dissection of a portion of DZ3a; this DZ was created by a single 30 keV W^+ projectile ion. The solid black dots indicate normal lattice sites and the open circles indicate vacancies in the $(8\bar{1}3)$ plane.

Figure 4: (a) The partial 211 stereographic projection showing the location of the depleted zones and dislocation loop detected in a specimen which had been irradiated with 30 keV Mo^+ ion parallel to the $\cong[\bar{8}\ 5\ 11]$ direction. (b) The corresponding cross-sectional view of the FIM tip.

Figure 5: A series of the micrographs out of 145 recorded during the atom-by-atom dissection of a portion of DZ4b; this DZ was created by a single 30 keV Mo^+ projectile ion. The solid black dots indicate normal lattice sites and the open circles indicate vacancies in the (622) plane.

Figure 6: OR TEP visualizations of three different DZs in 30 keV W^+, Mo^+ or Cr^+ ion-irradiated tungsten specimens. The rod connecting any two vacancies, in the OR TEP visualizations, is equal to the first nearest-neighbor distance (≈ 2.74 Å) in tungsten; the surrounding tungsten atoms were omitted for the sake of clarity. Each of the DZs is at approximately the same magnification -- note the 25 Å marker.

Figure 7: An OR TEP visualization of DZ2b which was created by a single 30 keV W^{+} projectile ion. This figure was constructed from experimental data with the aid of the OR TEP program. This program was also used to construct the DZs shown in fig. 6 and figs. 8-17.

Figure 8: An OR TEP visualization of DZ3a which was created by a single 30 keV W^{+} projectile ion.

Figure 9: An OR TEP visualization of DZ4d which was created by a single 30 keV Mo^{+} projectile ion.

Figure 10: An OR TEP visualization of DZ6a which was created by a single 30 keV Cu^{+} projectile ion.

Figure 11: An OR TEP visualization of DZ7a which was created by a single 30 keV Cu^{+} projectile ion.

Figure 12: An OR TEP visualization of DZ5a which was created by a single 30 keV Cr^{+} projectile ion.

Figure 13: An OR TEP visualization of DZ15b which was created by a single 15 keV Kr^{+} projectile ion.

Figure 14: An OR TEP visualization of DZ14b which was created by a single 30 keV Kr^{+} projectile ion.

Figure 15: An OR TEP visualization of DZ8a which was created by a single 45 keV Kr^{+} projectile ion.

Figure 16: An OR TEP visualization of DZ9a which was created by a single 60 keV Kr^{+2} projectile ion.

Figure 17: An OR TEP visualization of DZ13a which was created by a single 70 keV Kr^{+2} projectile ion.

Figure 18: A plot of the reduced stopping power [$S(\varepsilon)$] as a function of the reduced energy (ε). The curves labelled S_n (LSS) and S_n(WHB) are the nuclear (elastic) stopping power functions according to Linhard, Scharff and Schiøtt (1963) and Wilson, Haggmark and Bismarck (1977), respectively. The curves labeled S_e(Cr^+ on W) and S_e(W^+ on W) are the electronic (inelastic) stopping power curves according to Linhard's and Scharff's (1961) equation -- see eqns. (6) and (7).

Figure 19: A schematic diagram to illustrate the qualitative differences in the vacancy structure of DZs created by different projectile ions; see §4.1 for details.

Figure 20: A schematic diagram showing the zeroth (solid circles) and the first (open circles) layers of the (222) and (332) planes. This figure is used to explain how a depleted zone was reconstructed from the FIM images; see Appendix for details.

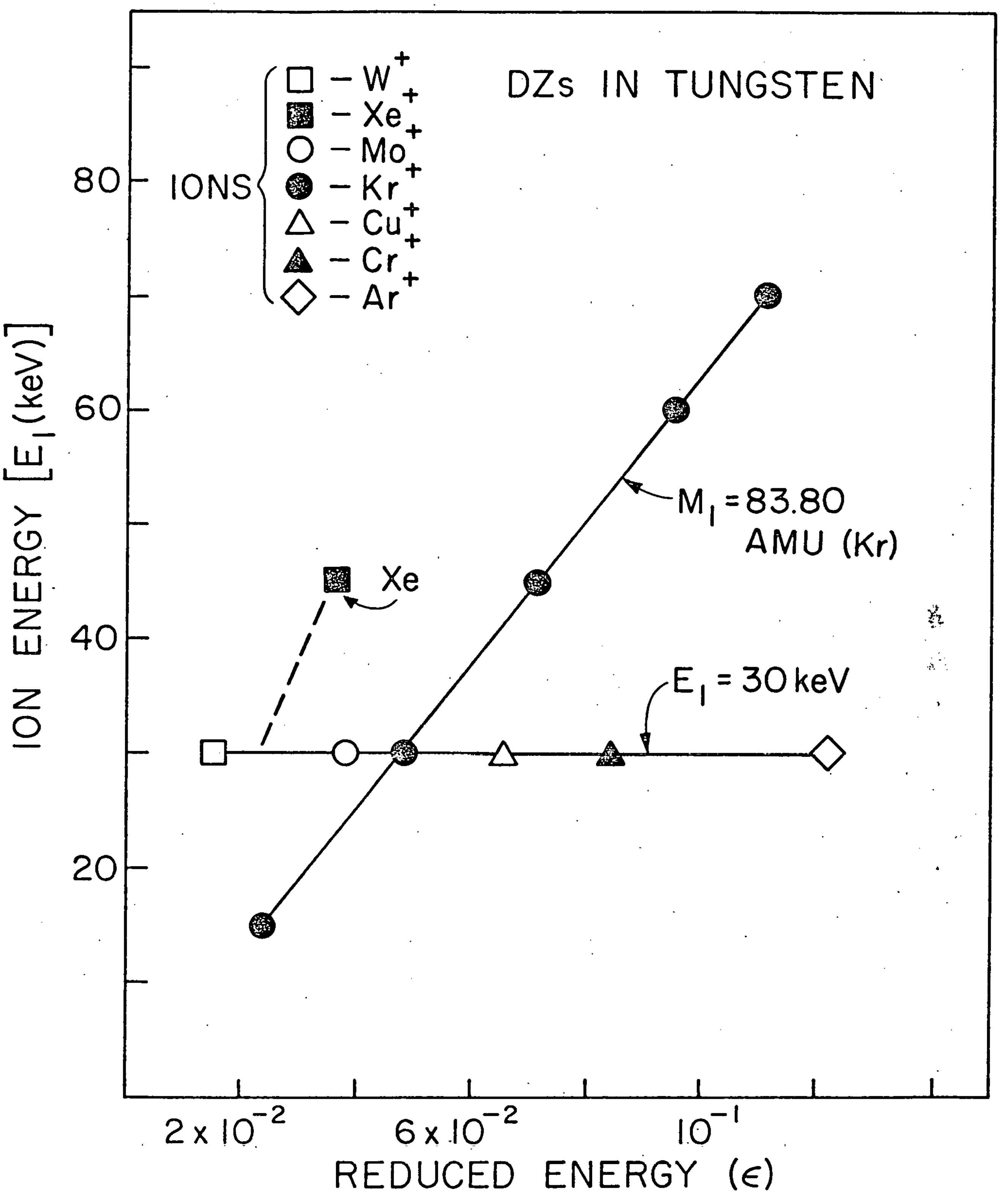
DZs IN TUNGSTEN
IONS
□ – W⁺
■ – Xe⁺
○ – Mo⁺
● – Kr⁺
△ – Cu⁺
▲ – Cr⁺
◇ – Ar⁺
Xe
M₁ = 83.80 AMU (Kr)
E₁ = 30 keV
ION ENERGY [E₁ (keV)]
80
60
40
20
2 x 10⁻²
6 x 10⁻²
10⁻¹
REDUCED ENERGY (ε)

Figure 1

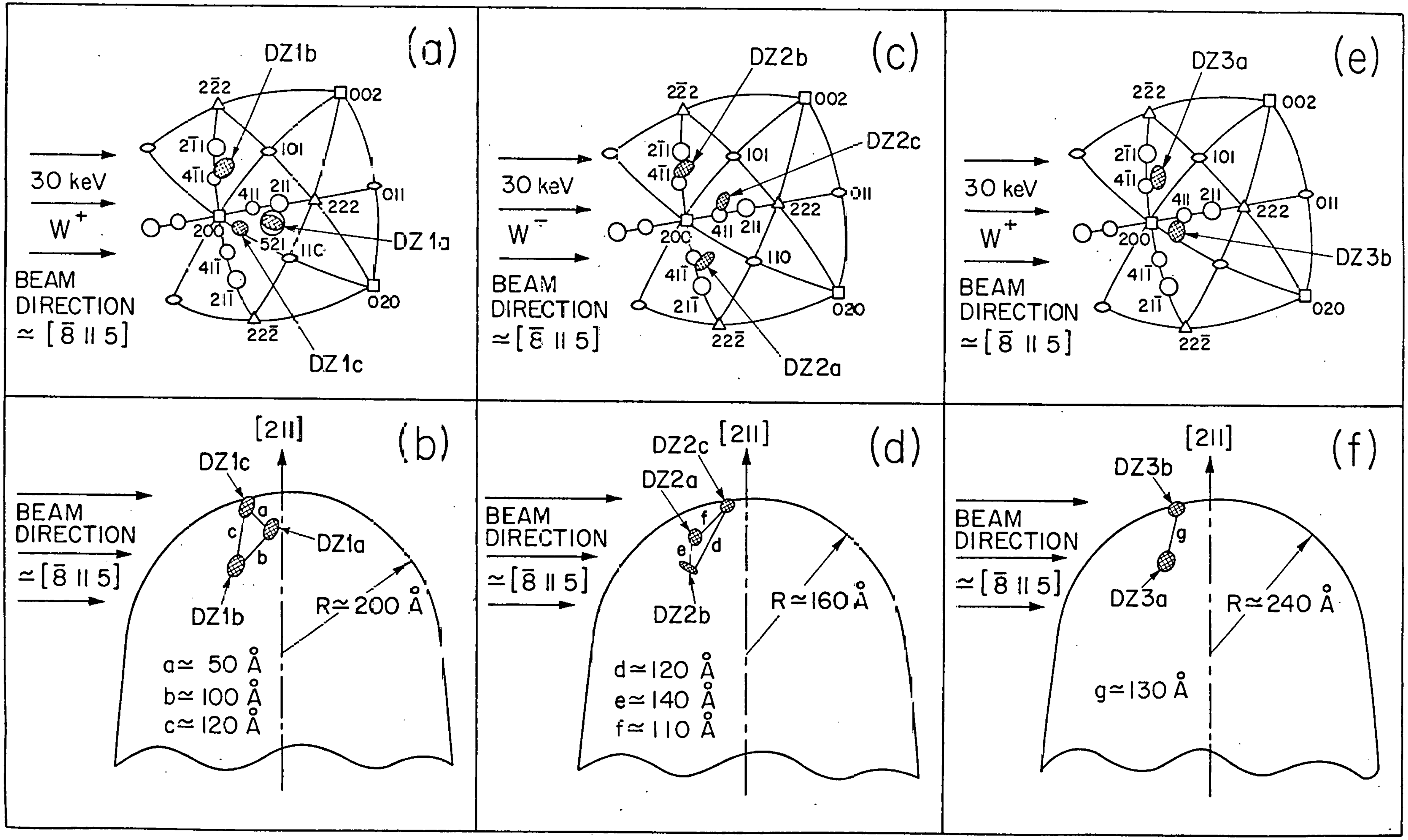

(a)
DZ1b
2$\bar{2}$2
002
2$\bar{1}$1
101
4$\bar{1}$1
411
211
011
222
200
521
DZ1a
110
4$1\bar{1}$
2$1\bar{1}$
020
22$\bar{2}$
DZ1c
30 keV
W$^+$
BEAM DIRECTION
≃ [$\bar{8}$ 11 5]
(c)
DZ2b
2$\bar{2}$2
002
DZ2c
2$\bar{1}$1
101
4$\bar{1}$1
011
222
200
411
211
110
4$1\bar{1}$
2$1\bar{1}$
020
22$\bar{2}$
DZ2a
30 keV
W$^+$
BEAM DIRECTION
≃[$\bar{8}$ 11 5]
(e)
DZ3a
2$\bar{2}$2
002
2$\bar{1}$1
101
4$\bar{1}$1
411
211
011
222
200
DZ3b
4$1\bar{1}$
2$1\bar{1}$
020
22$\bar{2}$
30 keV
W$^+$
BEAM DIRECTION
≃[$\bar{8}$ 11 5]
(b)
[211]
DZ1c
a
c
DZ1a
b
DZ1b
BEAM DIRECTION
≃[$\bar{8}$ 11 5]
R≃200 Å
a≃ 50 Å
b≃ 100 Å
c≃ 120 Å
(d)
DZ2c
[211]
DZ2a
f
e
d
DZ2b
BEAM DIRECTION
≃[$\bar{8}$ 11 5]
R≃160 Å
d≃120 Å
e≃140 Å
f≃110 Å
(f)
[211]
DZ3b
g
DZ3a
BEAM DIRECTION
≃[$\bar{8}$ 11 5]
R≃240 Å
g≃130 Å

Figure 2

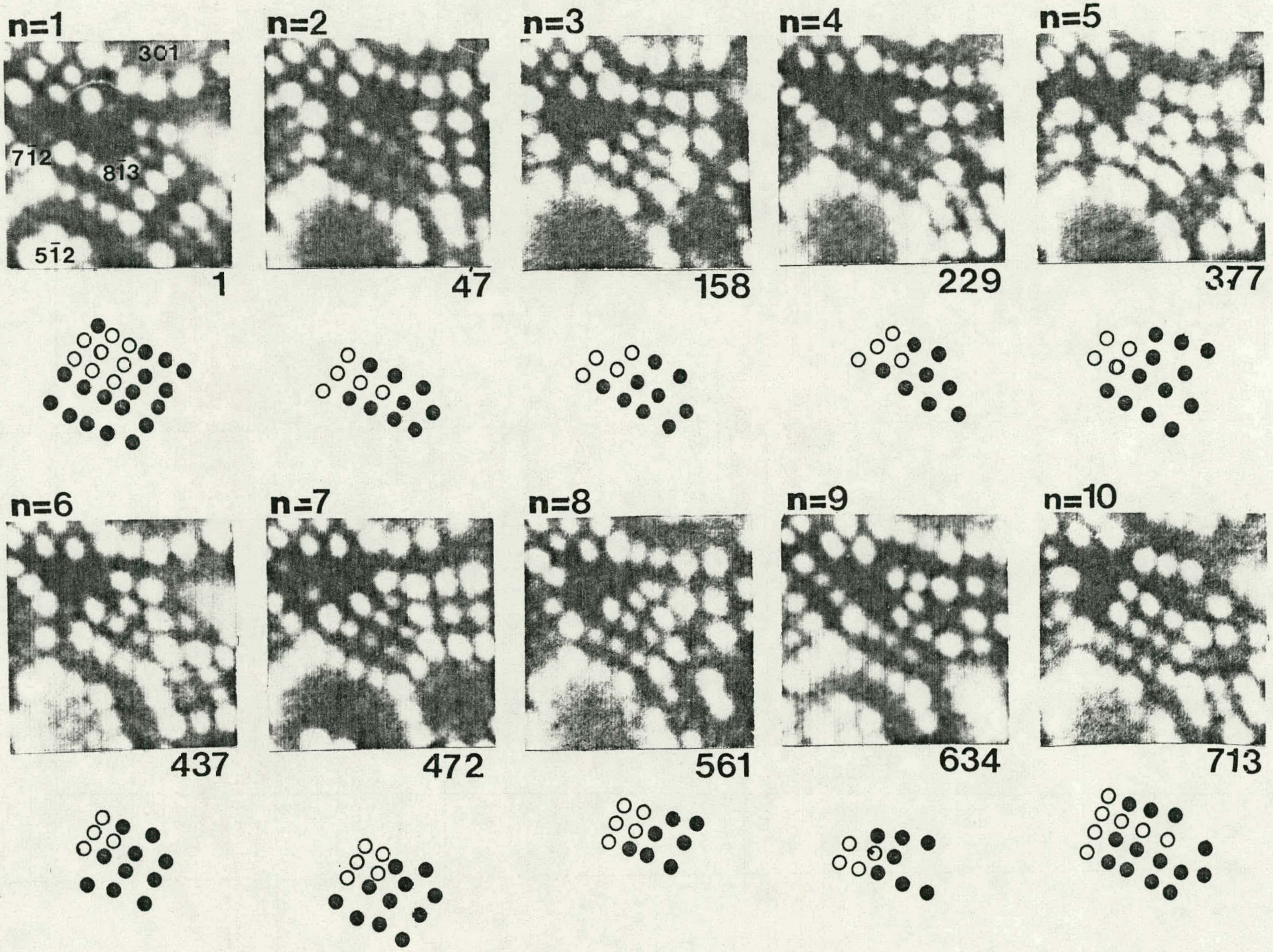
n=1
301
71̄2
81̄3
51̄2
1
n=2
47
n=3
158
n=4
229
n=5
377
n=6
437
n=7
472
n=8
561
n=9
634
n=10
713

Figure 3

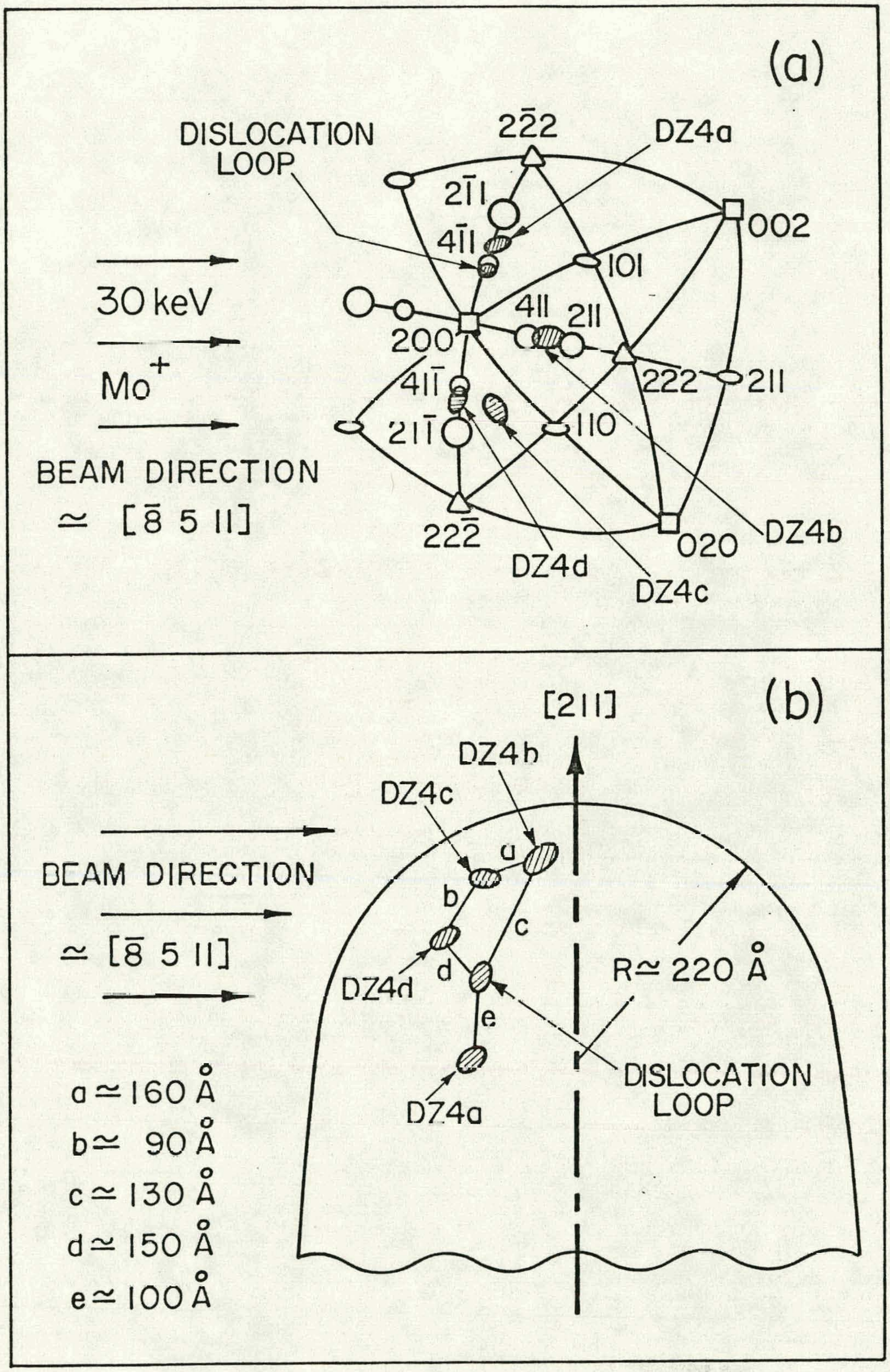
(a)
DISLOCATION LOOP
2$\bar{2}$2
DZ4a
2$\bar{1}$1
4$\bar{1}$1
002
101
30 keV
Mo$^+$
411
211
200
222
211
4$1\bar{1}$
21$\bar{1}$
110
BEAM DIRECTION
≃ [$\bar{8}$ 5 11]
22$\bar{2}$
020
DZ4b
DZ4d
DZ4c
(b)
[211]
DZ4b
DZ4c
a
b
c
d
e
DZ4d
DZ4a
BEAM DIRECTION
≃ [$\bar{8}$ 5 11]
R ≃ 220 Å
DISLOCATION LOOP
a ≃ 160 Å
b ≃ 90 Å
c ≃ 130 Å
d ≃ 150 Å
e ≃ 100 Å

Figure 4

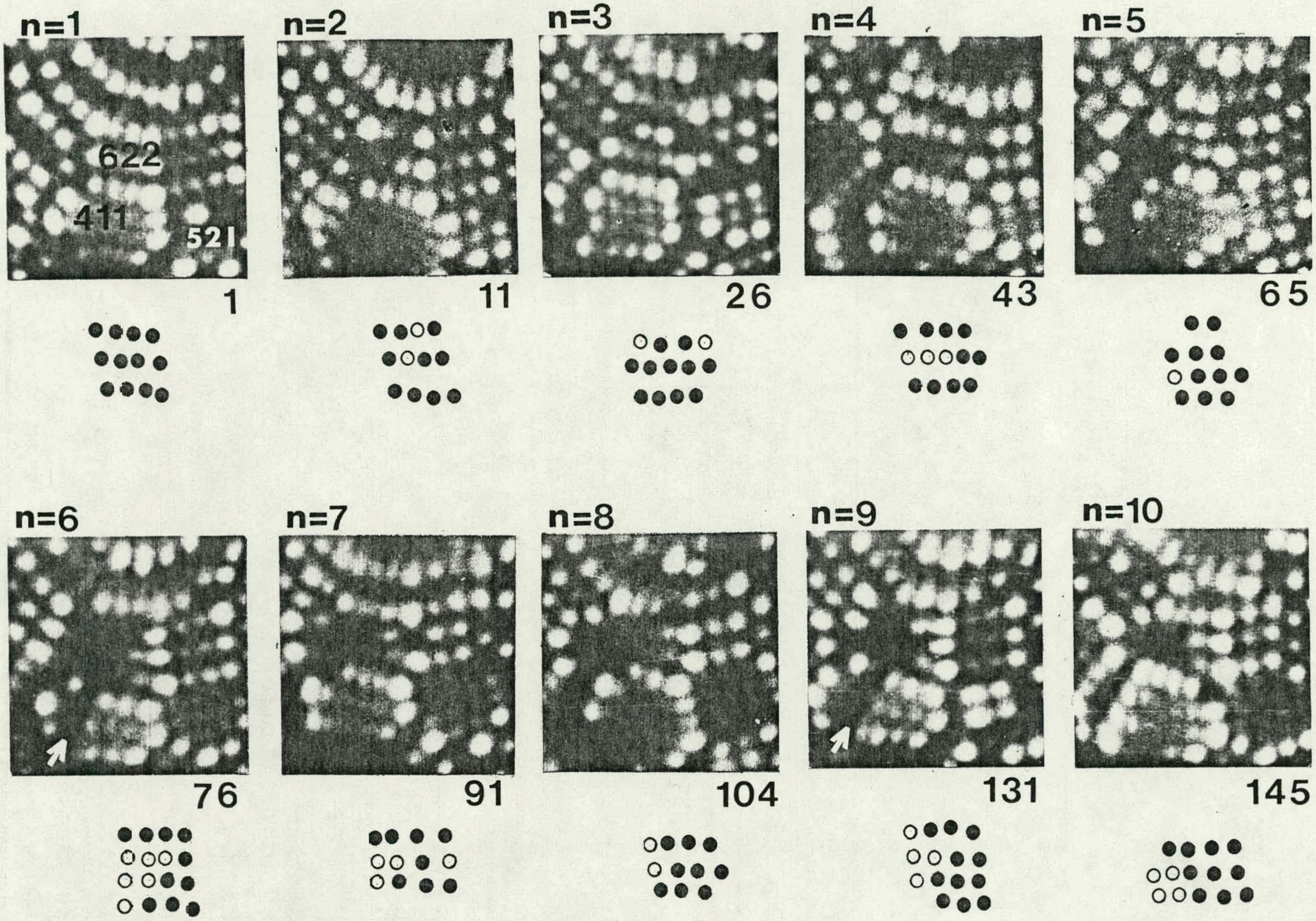
n=1
622
411
521
1
n=2
11
n=3
26
n=4
43
n=5
65
n=6
76
n=7
91
n=8
104
n=9
131
n=10
145

Figure 5

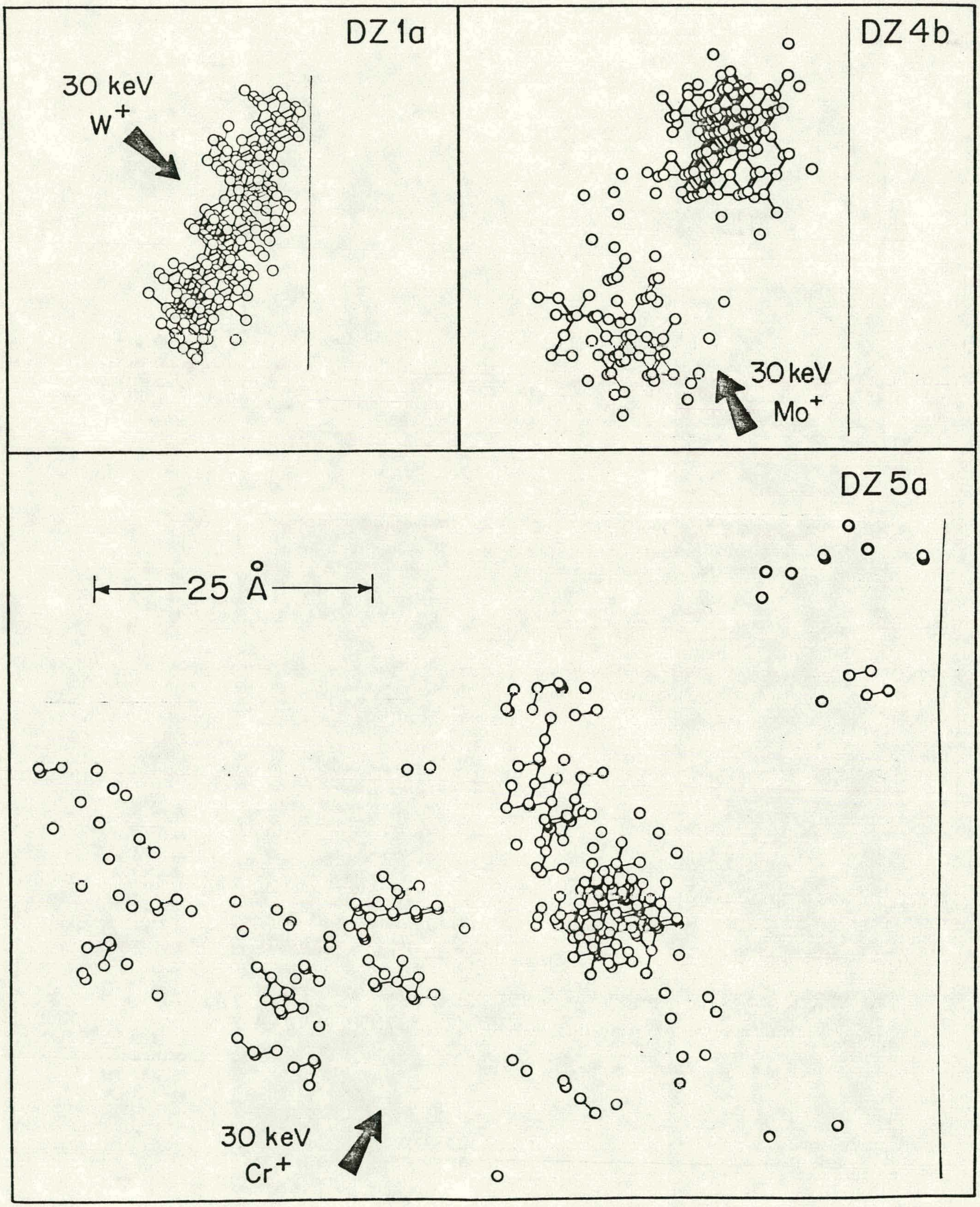

Figure 6

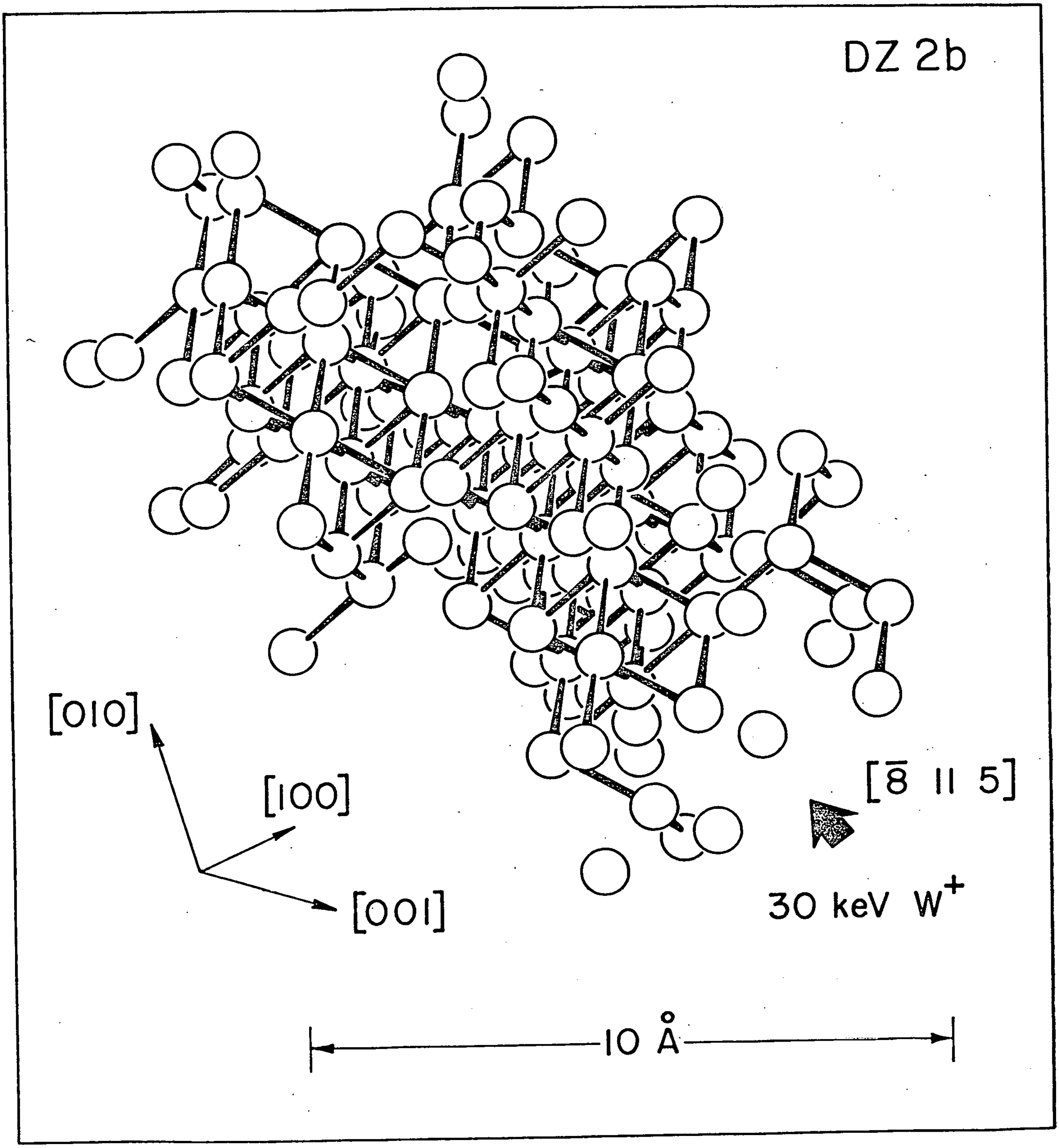

Figure 7

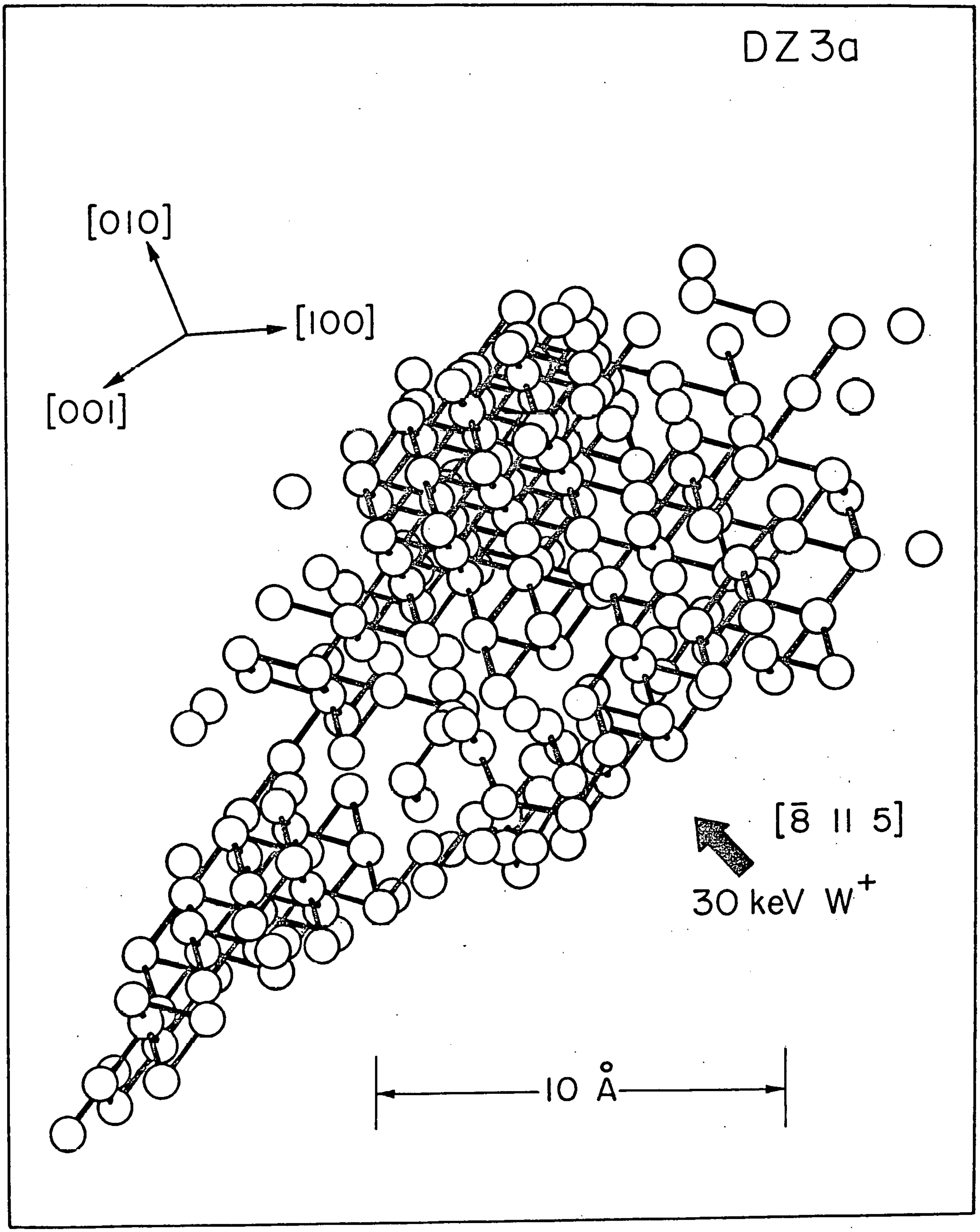

Figure 8

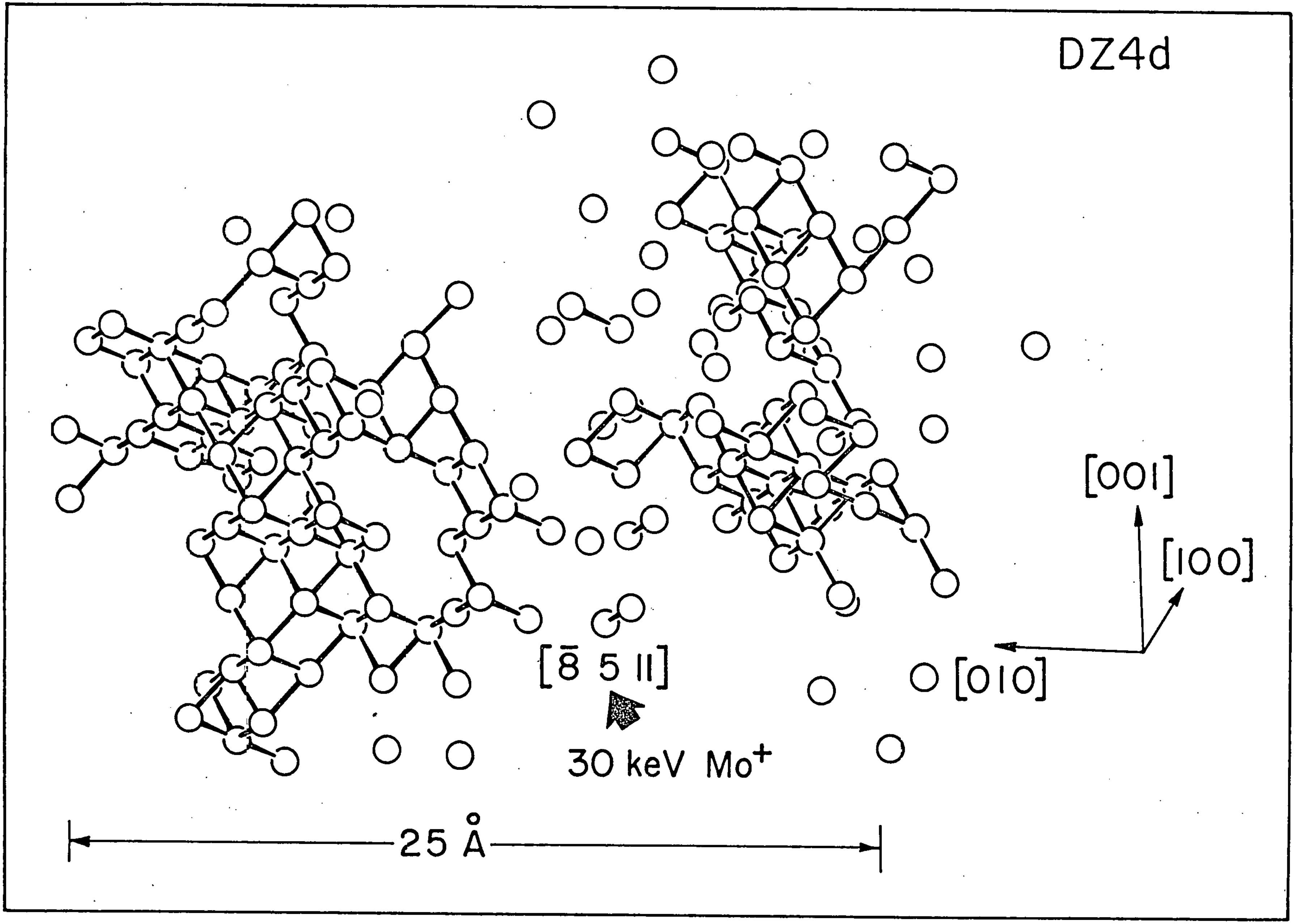

Figure 9

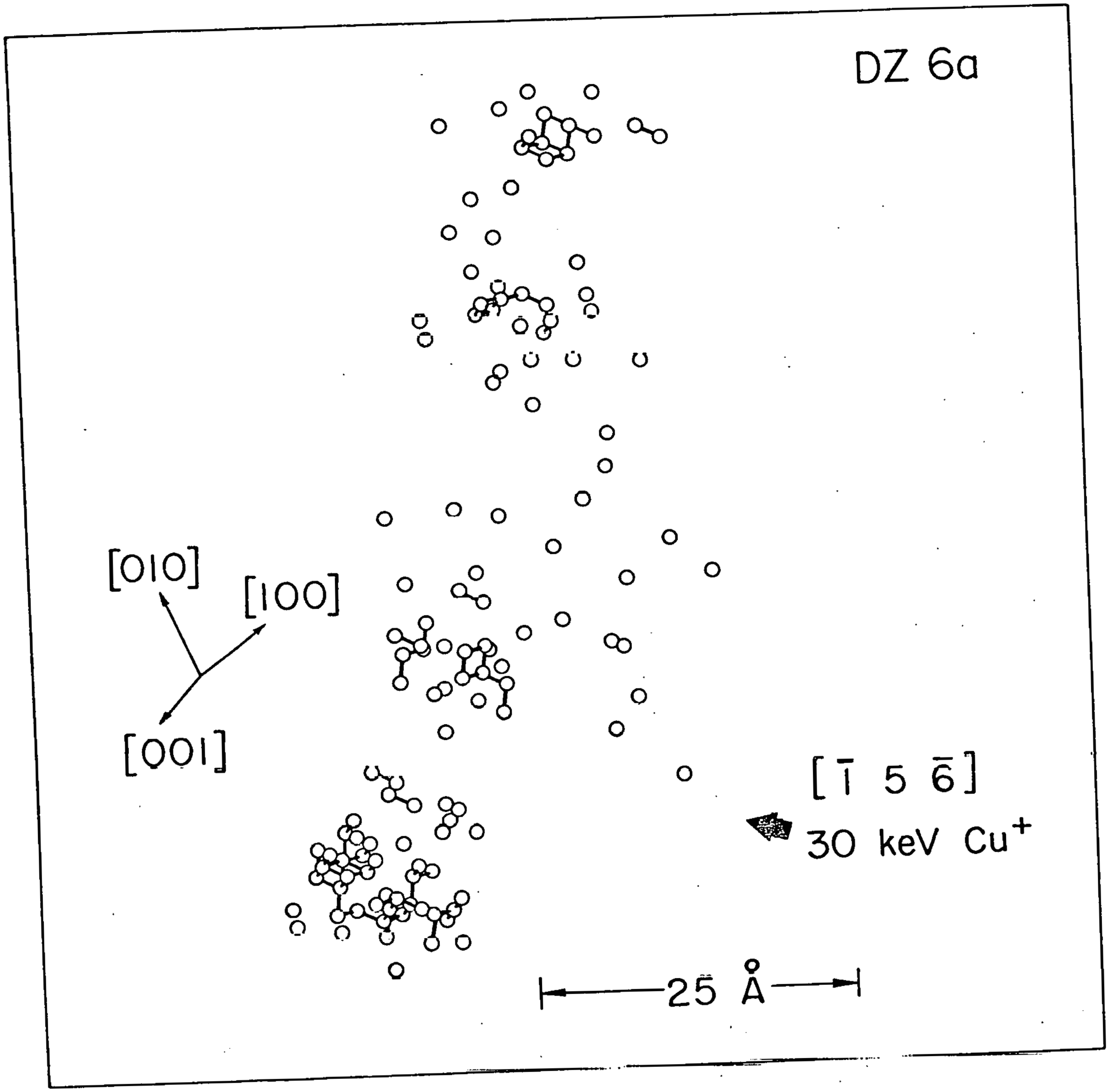

Figure 10

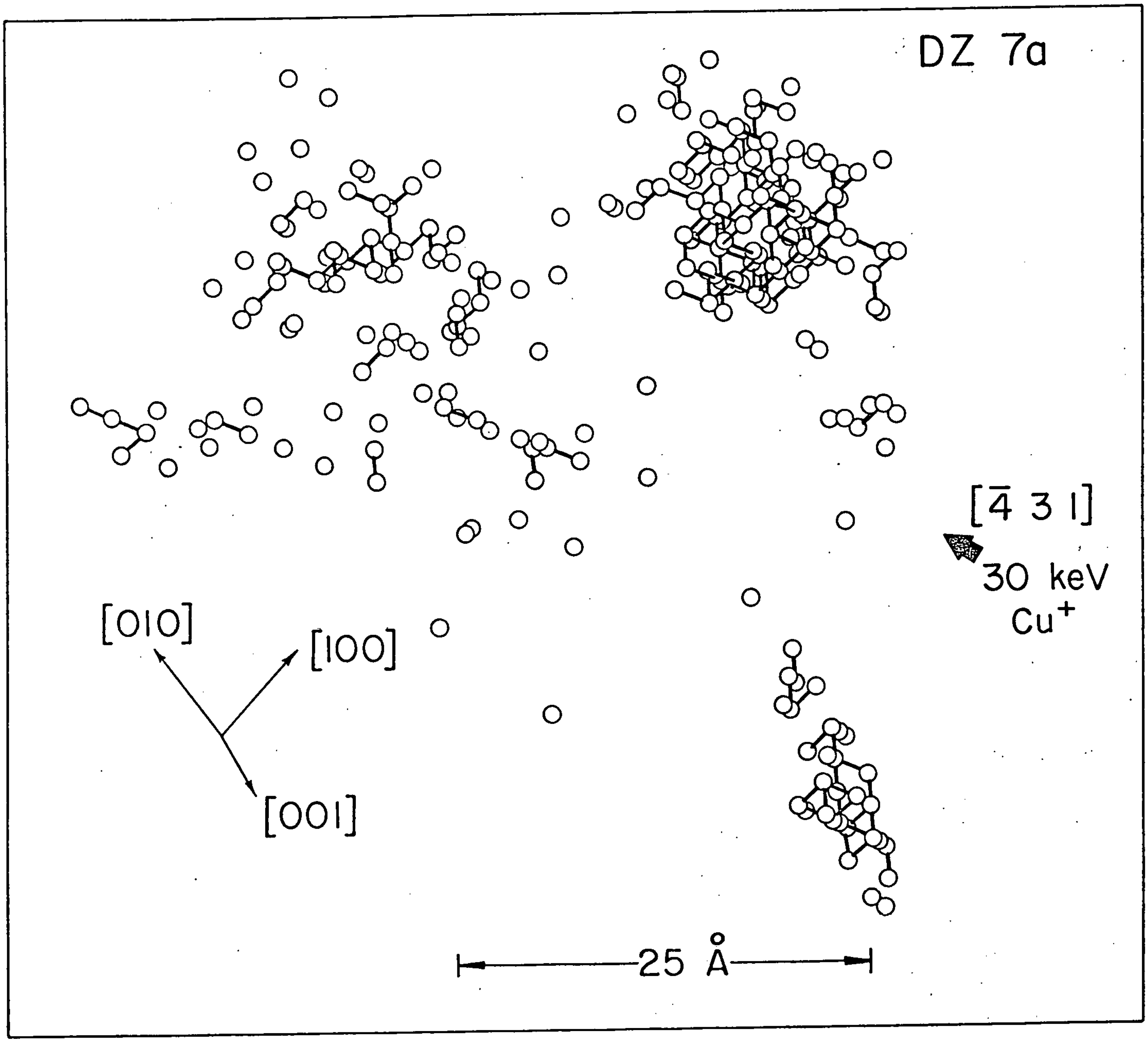

Figure 11

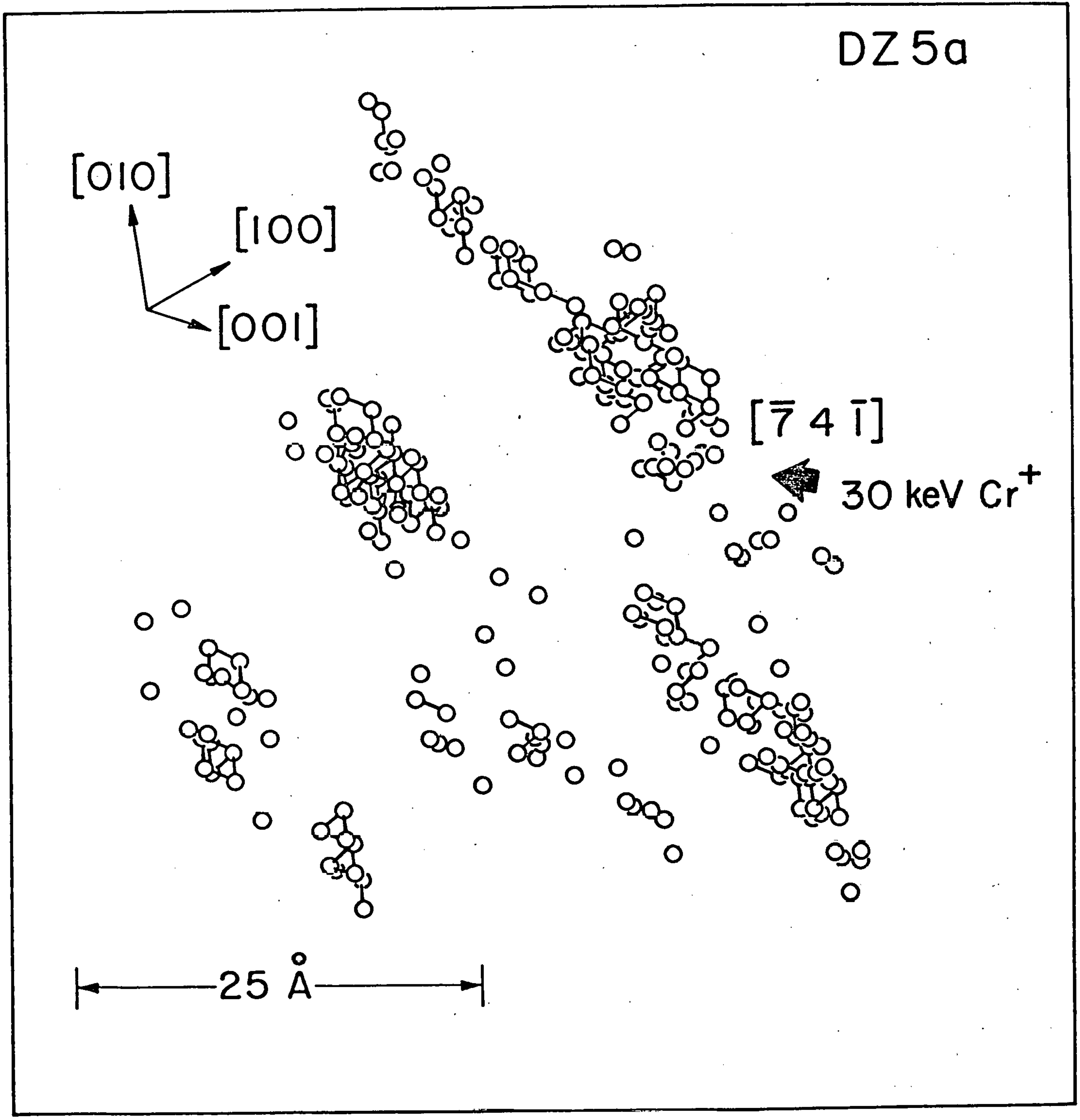

Figure 12

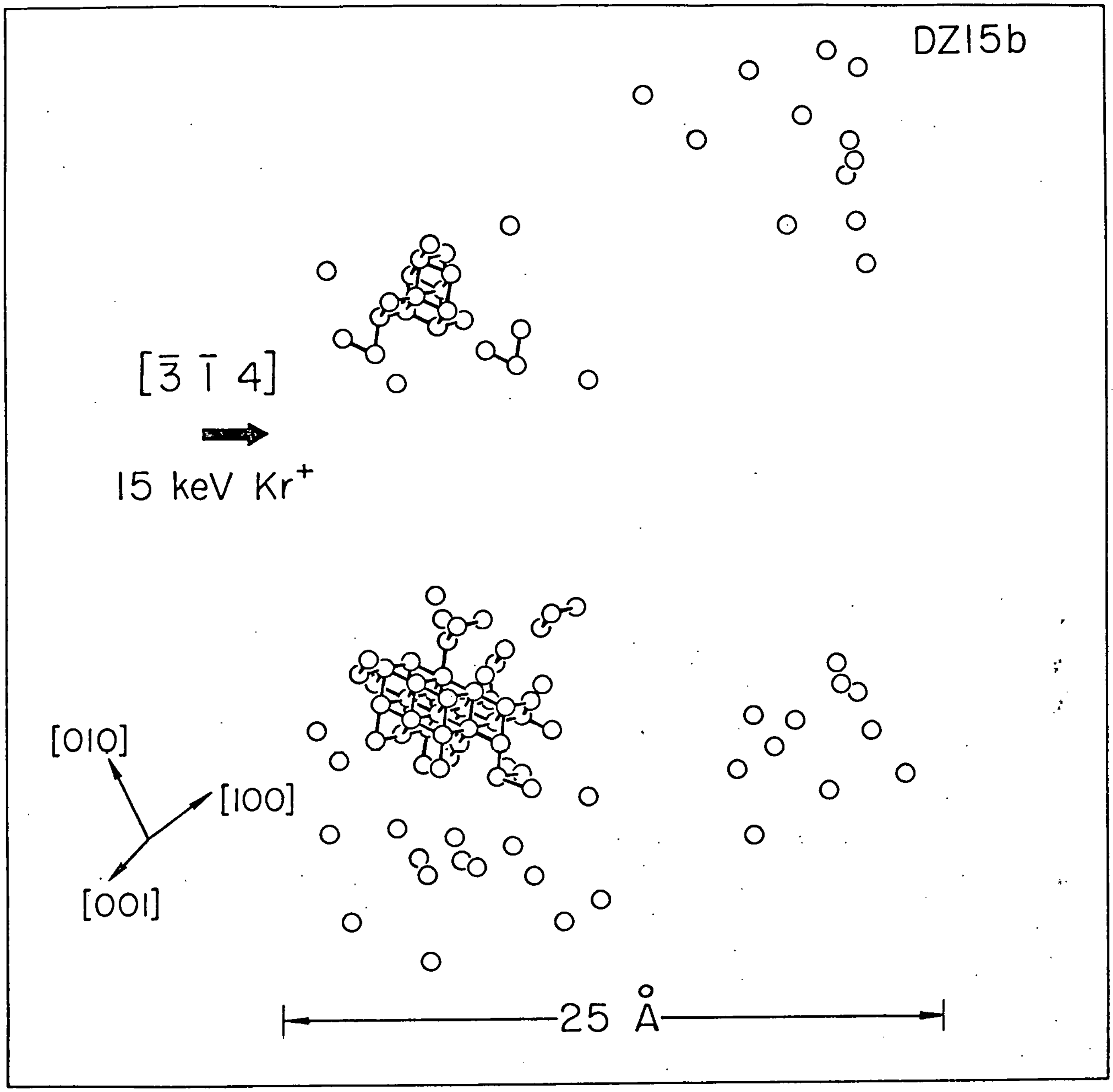

Figure 13

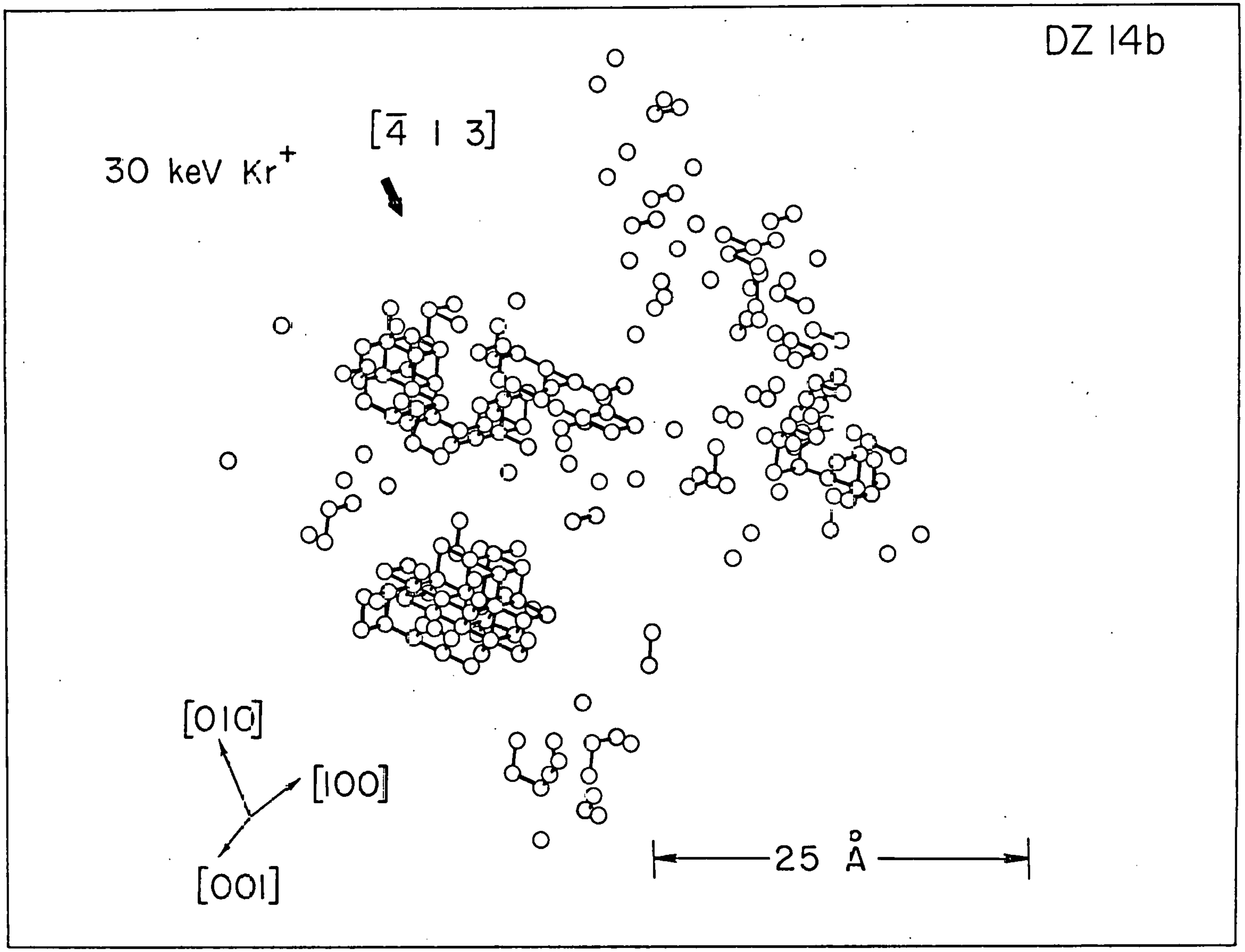

Figure 14

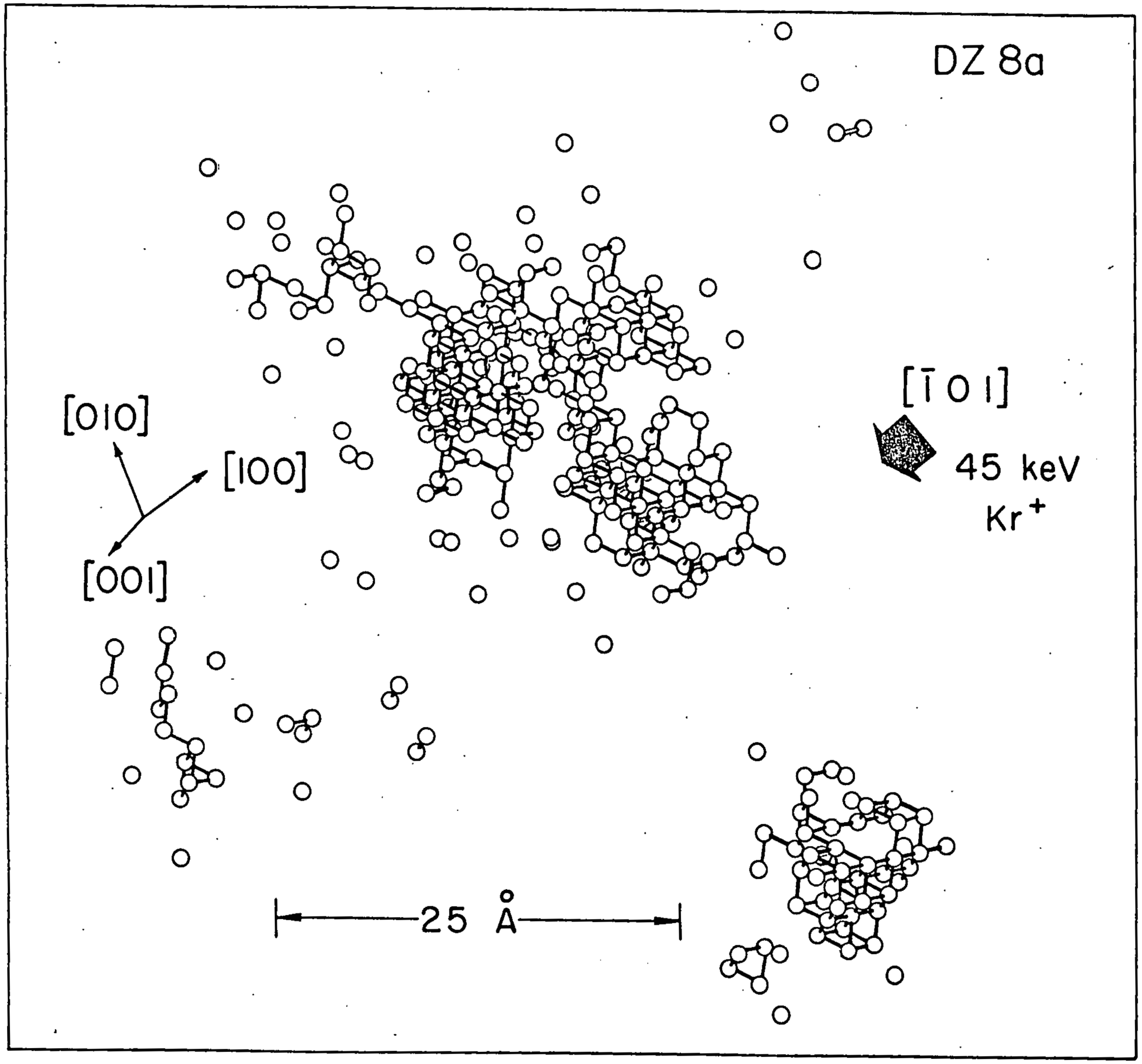

Figure 15

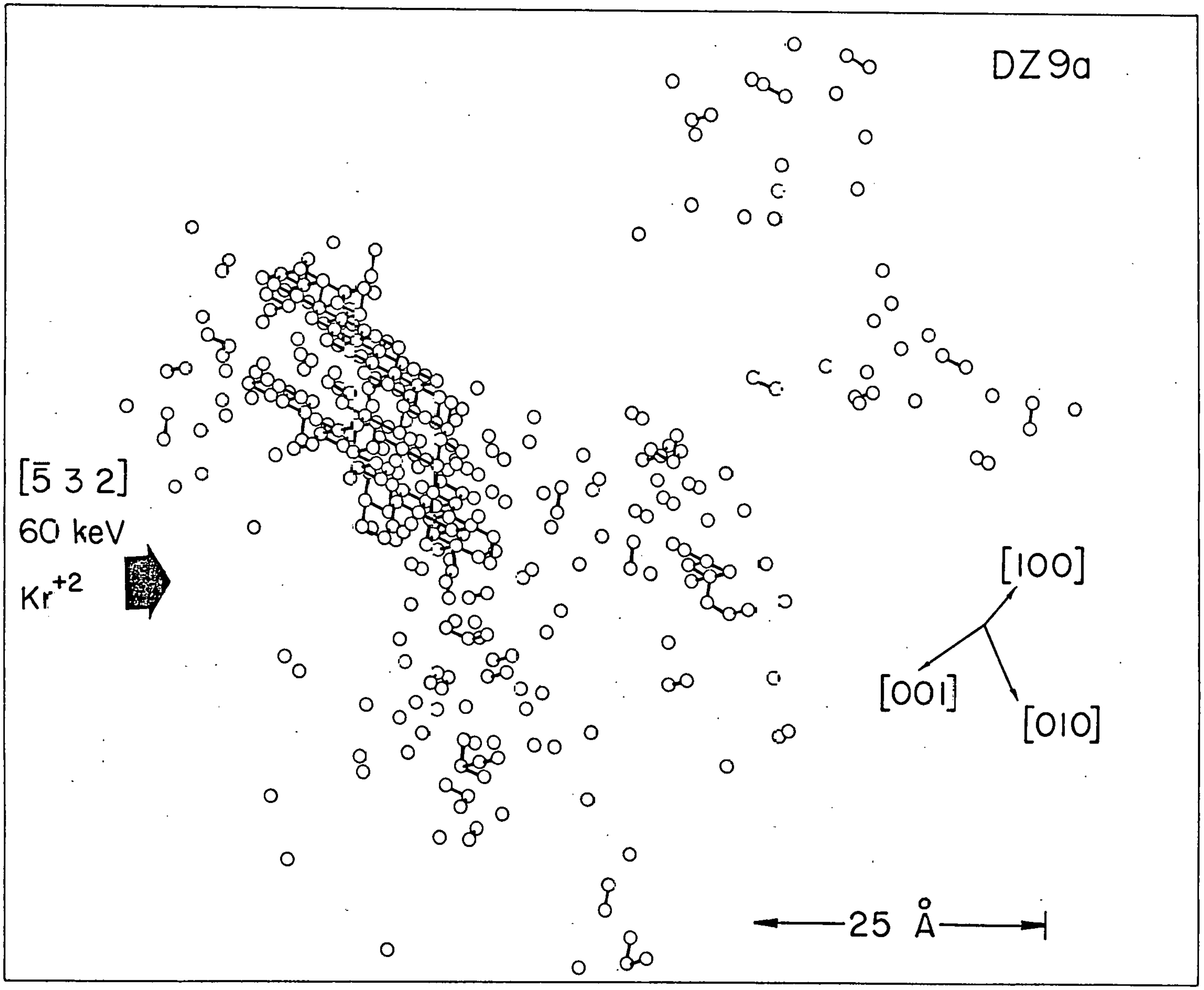

Figure 16

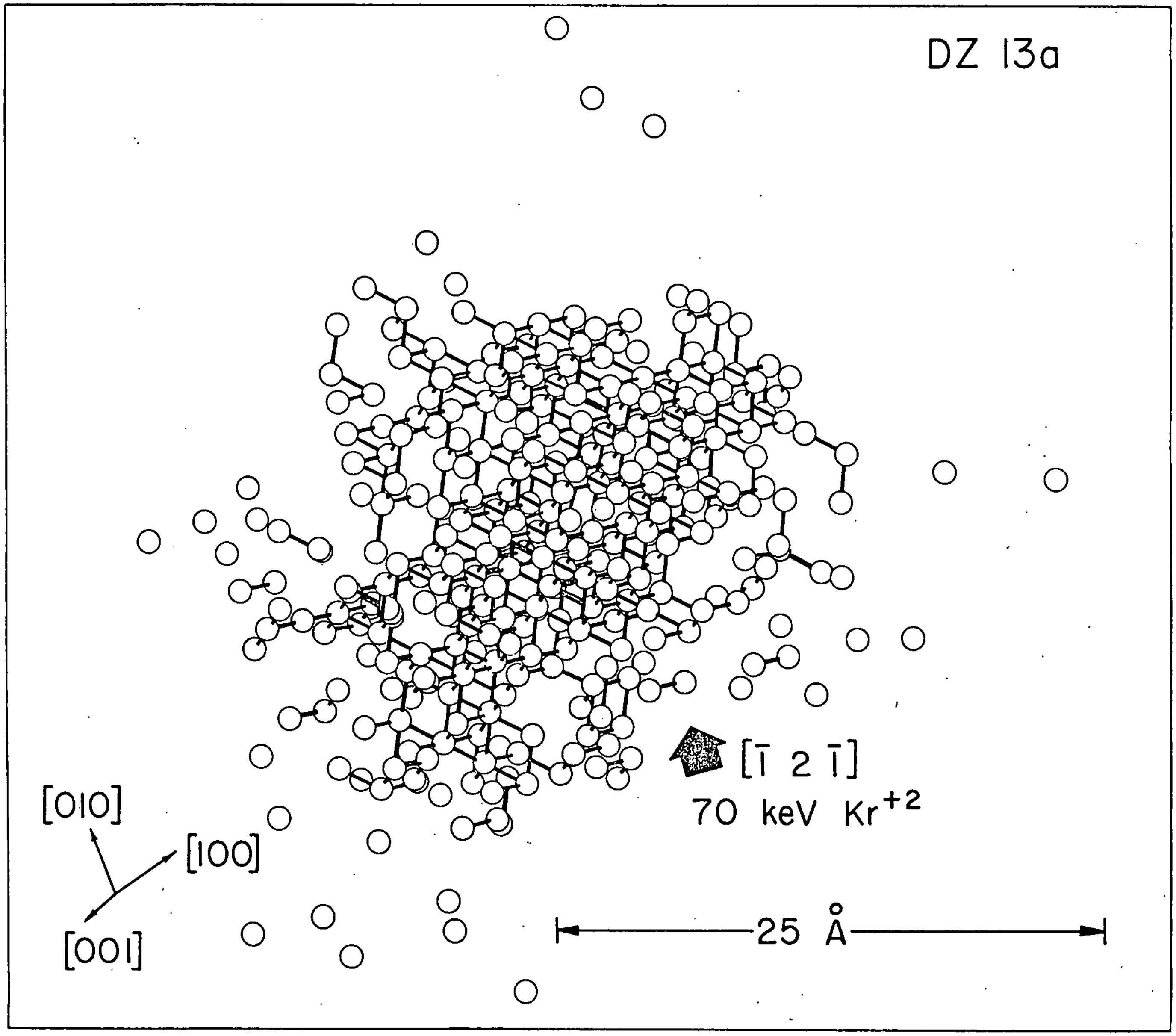

Figure 17

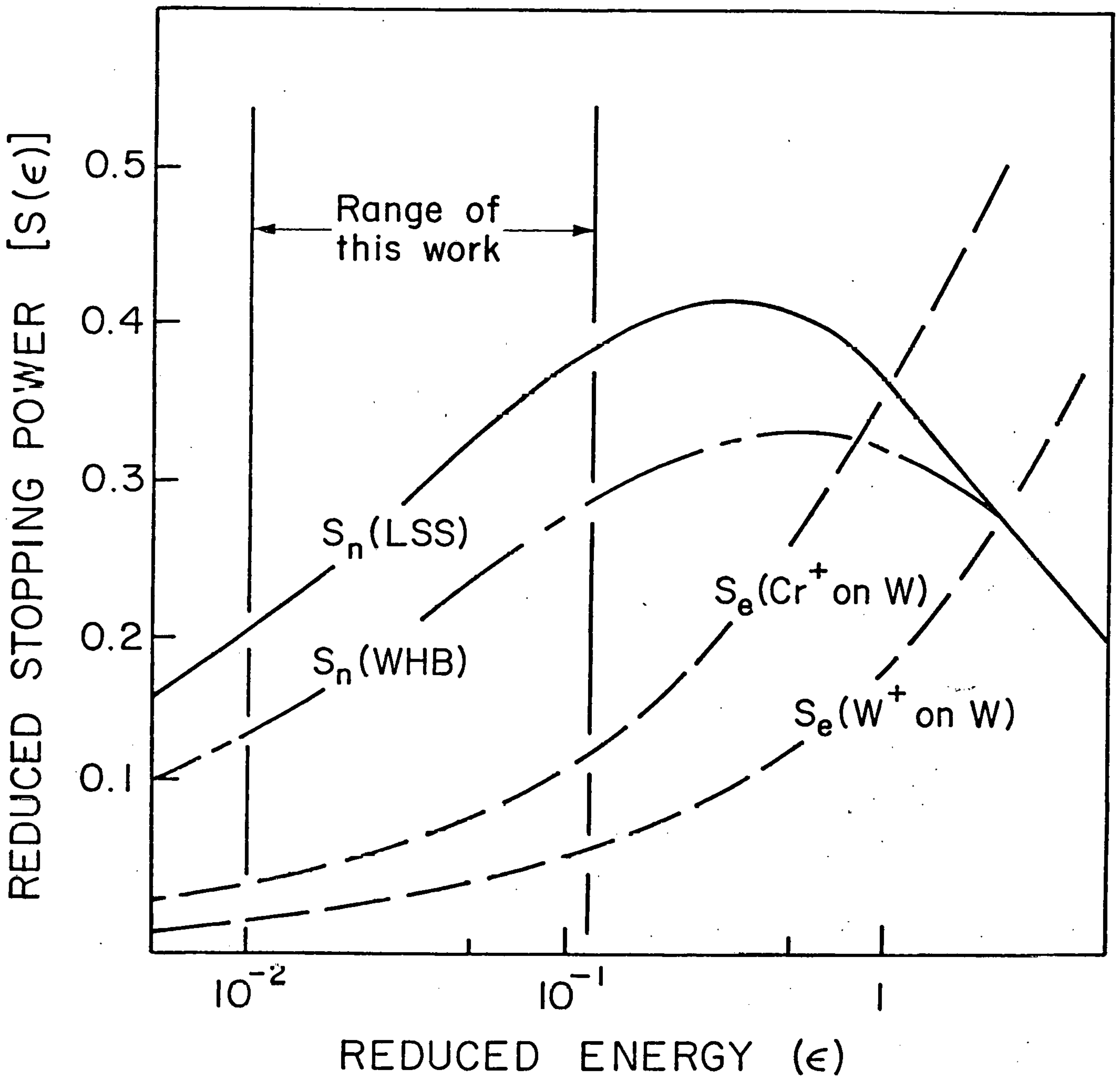
REDUCED STOPPING POWER [S(ε)]
0.5
0.4
0.3
0.2
0.1
Range of this work
S_n(LSS)
S_n(WHB)
S_e(Cr^+ on W)
S_e(W^+ on W)
10^{-2}
10^{-1}
1
REDUCED ENERGY (ε)

Figure 18

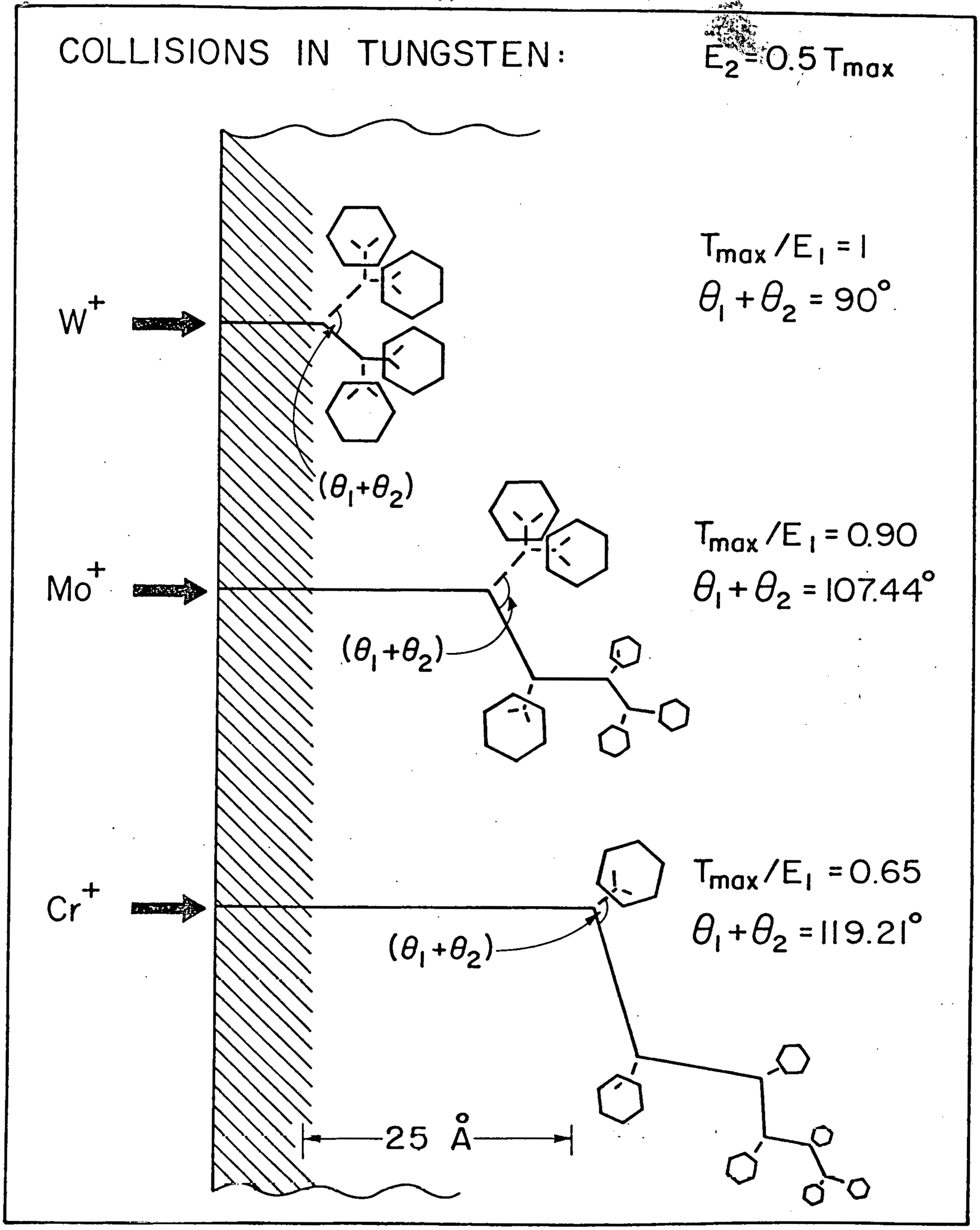
COLLISIONS IN TUNGSTEN:
$E_2 = 0.5\,T_{max}$
W^+
$T_{max}/E_1 = 1$
$\theta_1 + \theta_2 = 90°$
$(\theta_1+\theta_2)$
Mo^+
$T_{max}/E_1 = 0.90$
$\theta_1 + \theta_2 = 107.44°$
$(\theta_1+\theta_2)$
Cr^+
$T_{max}/E_1 = 0.65$
$\theta_1 + \theta_2 = 119.21°$
$(\theta_1+\theta_2)$
25 Å

Figure 19

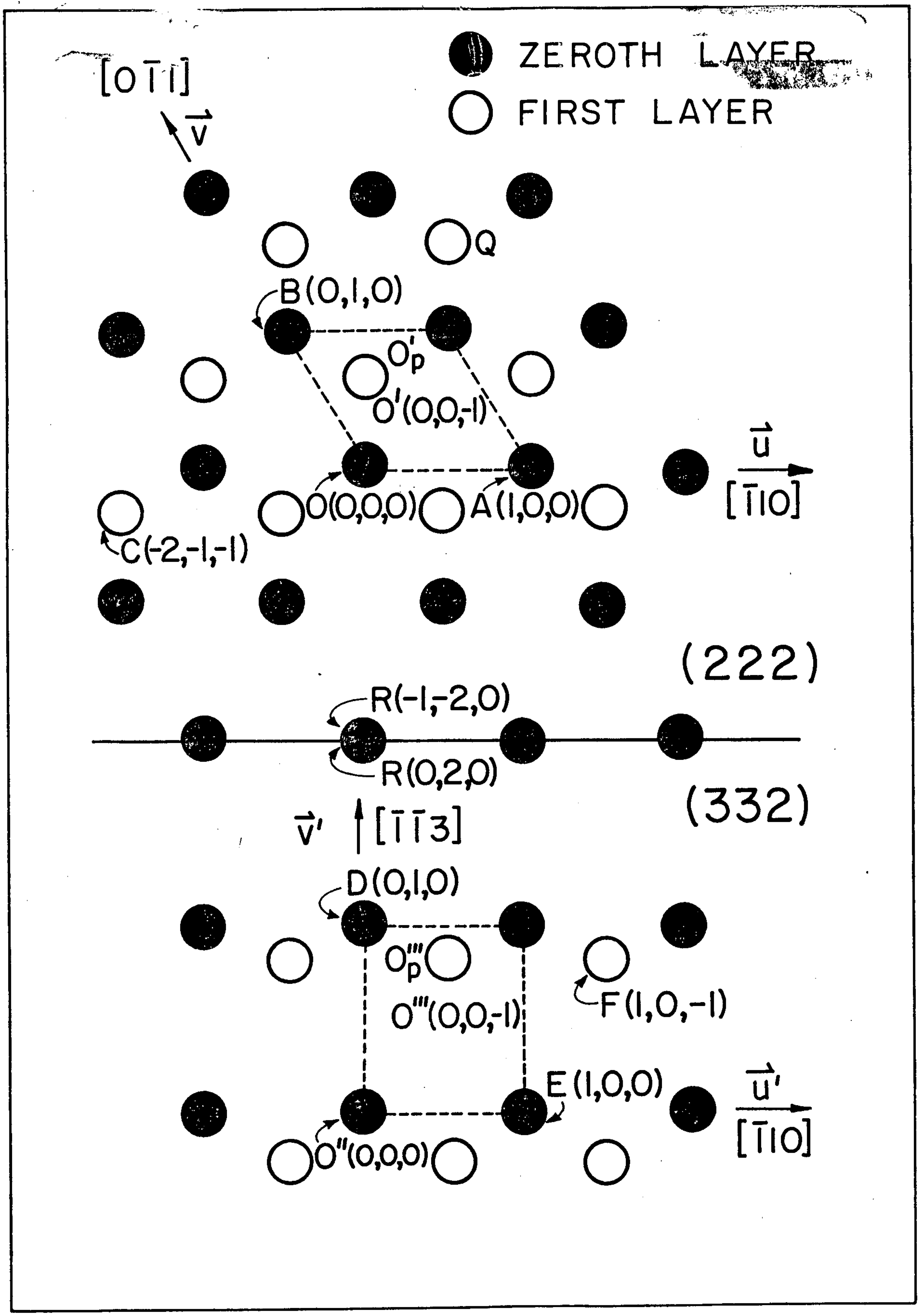

● ZEROTH LAYER
○ FIRST LAYER
[0 1̄ 1̄]
v⃗
Q
B(0,1,0)
O'p
O'(0,0,-1)
u⃗
[1̄10]
O(0,0,0)
A(1,0,0)
C(-2,-1,-1)
(222)
R(-1,-2,0)
R(0,2,0)
(332)
v⃗'
[1̄ 1̄ 3]
D(0,1,0)
O'''p
O'''(0,0,-1)
F(1,0,-1)
E(1,0,0)
u⃗'
[1̄10]
O''(0,0,0)

Figure 20